The PVEMC Experiment

First Measurement of the Flavor Dependence of Nuclear PDF Modification Using Parity-Violating Deep Inelastic Scattering

A Proposal to PAC 50

Spokespersons: John Arrington, Rakitha Beminiwattha, Dave Gaskell, Juliette Mammei, Paul E. Reimer

May 15, 2022

J. Arrington[*,†], T. J. Hague, S. Li, E. Sichtermann, Y. Mei
Lawrence Berkeley National Laboratory

R. Beminiwattha[*], S. P. Wells, N. Simicevic
Louisiana Tech University

D. Gaskell[*], J. Benesch, A. Camsonne, J. P. Chen, S. Covrig, J.-O. Hansen, C. E. Keppel, and M.M. Dalton, R. Michaels
Thomas Jefferson National Accelerator Facility

J. Mammei[*], W. Deconinck, M. Gericke, P. Blunden
University of Manitoba

P. E. Reimer[*], W. R. Armstrong, I. C. Cloët
Argonne National Laboratory

S. Barkanova
Acadia University

K. Aniol
California State University, Los Angeles

D. S. Armstrong
College of William and Mary

H. Gao, X. Li, T. Liu, C. Peng, W. Xiong, X. Yan, and Z. Zhao
Duke University

P. Markowitz and M. Sargsian
Florida International University

A. Aleksejevs
Grenfell Campus of Memorial University

D. McNulty
Idaho State University

V. Bellini, C. Sutera
INFN - Sezione di Catania

J. Beričič, S. Širca, and S. Štajner
Jožef Stefan Institute and University of Ljubljana, Slovenia

J. Dunne, D. Dutta and L. El Fassi
Mississippi State University

P. M. King and J. Roche
Ohio University, Athens, Ohio

M. Hattawy
Old Dominion University, Norfolk, Virginia

R. Gilman, K. E. Mesick
Rutgers University

A. Deshpande, C. Gal, N. Hirlinger Saylor, T. Kutz, and Y.X. Zhao
Stony Brook University

R. Holmes and P. Souder
Syracuse University

A. W. Thomas
University of Adelaide, Australia

Y. Kolomensky

University of California, Berkeley

A. J. Puckett
University of Connecticut

K. S. Kumar, R. Miskimen
University of Massachusetts, Amherst

N. Fomin
University of Tennessee, Knoxville

X. Bai, D. Di, K Gnanvo, C. Gu, N. Liyanage, H. Nguyen, K. D. Paschke, V. Sulkosky, and X. Zheng
University of Virginia

N. Kalantarians
Virginia Union University

and the SoLID Collaboration

*Spokesperson
†Contact, JArrington@lbl.gov

Contents

1 Executive Summary

We propose a clean and precise measurement of the flavor dependence of the EMC effect using parity-violating deep inelastic scattering on a ^{48}Ca target. While the EMC effect has been known for almost 40 years, it is still not fully understood theoretically and there are essentially no reliable experimental constraints on its flavor dependence. This measurement will provide an extremely sensitive test for flavor dependence in the modification of nuclear pdfs for neutron-rich nuclei. A measurement of the flavor dependence will provide new and important information and help to elucidate nucleon modification at the quark level. In addition to helping understand the origin of the EMC effect, a flavor-dependent nuclear pdf modification could have significant impact on a range of processes, including neutrino-nucleus scattering, nuclear Drell-Yan processes, or e-A observables at the Electron-Ion Collider.

Parity-violating deep inelastic scattering generates an asymmetry between helicity states of longitudinally polarized electrons scattered from a ^{48}Ca unpolarized target. This asymmetry arises from the interference between the virtual photon and Z^0 exchange and is effectively the ratio of weak to electromagnetic interactions between the target and electrons. In the quark-parton model it is directly sensitive to the ratios of quark flavors, and so is independent of the size of the flavor-independent EMC effect. Such a measurement is cleanly interpretable with minimal model dependence and offers the best direct access with available experimental techniques.

We propose to measure the parity-violating asymmetry $A_{\rm PV}$ from ^{48}Ca using 11 GeV beam at 80 μA and the SoLID detector in its PVDIS configuration. The only change from the PVDIS running conditions is the use of a ^{48}Ca target. With 68 days of data taking, we will obtain 0.7-1.3% statistical precision for $0.2 < x < 0.7$ with 0.6-0.7% systematic uncertainties. Based on the prominent CBT (Cloet-Bentz-Thomas) model of medium modification [1, 2], this would provide a measurement of the flavor dependence at well above the 6σ level (as seen in Fig. 1). While such models provide useful guidance contextualizing the significance of the measurement, the goal is not to test specific models, but to make a first measurement of the completely unknown flavor dependence of the EMC effect. In addition to providing exceptional discovery potential, the precision of the measurement will allow for quantification of the flavor-dependent effects, greatly improving our ability to differentiate between models of the EMC effect.
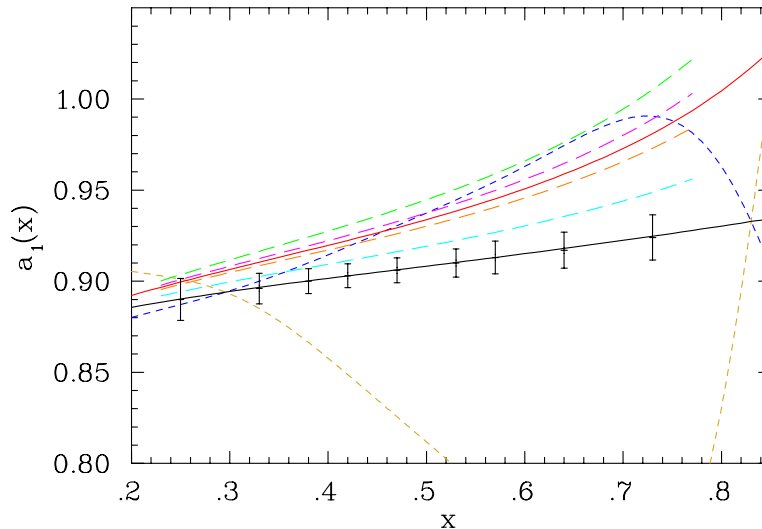

Figure 1: Projected uncertainties for the proposed measurement compared to models that include flavor-dependent EMC effect contributions, as summarized in Sec. 2 and described in detail in Sec. 4.2.

2 Summary of key updates to the proposal

The overall goals and general methods of this proposal are unchanged from the previous submission. However, the text has been reorganized and expanded in some sections to clarify important details and additional tests have been performed to address questions that arose at PAC49. We provide here a brief summary of the key updates to the proposal.

1. Calcium-48 target: Working with the target group, we modified the design of the target in a way that allows the same effective target thickness while cutting the amount of ^{48}Ca needed by 30% or more. This reduces the amount of calcium required to the point where the target can be made using the lab's existing supply of ^{48}Ca, assuming efficient reprocessing of the material. The costs involved should be limited to the cost of reprocessing the existing material, plus (perhaps) a small amount of new material if the recovery is less efficient than estimates. Details of the updated target design are presented in Sec. 5.1. This would give us a ^{48}Ca purity of 93% rather than the 95% assumed in the previous proposal, and we have increased the running time by 2 days to make up for the reduced enrichment.

2. Radiation: We have evaluated the radiation dose in the hall and at the site boundary in two ways: scaling the PVDIS radiation calculations to the PVEMC conditions, and by performing detailed Geant4 simulations with input from the Jefferson Lab Radiation Control Group. We also compare Geant4 estimates calculated for the conditions of other high-radiation experiments to the measured doses from the real data taking period as a check of the calculations and find that measured doses are typically a factor of $\sim$2 below the calculation. Based on all of these estimates, we believe the radiation dose in the hall and at the boundary will not be an issue for the requested beam time with ^{48}Ca. We have added a new section 7 which describes all of these estimates and discusses the expected impact on the magnet, electronics, and calorimeter.

3. Sensitivity studies: The question of the flavor dependence of the EMC effect has been an extremely important and active topic over the past few years [3, 4, 5, 6, 7, 8, 9, 10] and it is clear that the flavor dependence of the EMC effect could impact a wide range of measurements at Jefferson Lab, Fermilab, and a future EIC (as detailed in Sec. 3.4), as well as providing important information to help constrain the origin of the EMC effect and the origin of the EMC-SRC correlation. However, it has also become clear that the inclusive cross section ratio measurements have only very limited sensitivity to the flavor dependence [11, 6]. There has been a great deal of activity attempting to identify reliable experimental tests of flavor dependence and to evaluate their impact on other measurements [12], highlighting the importance of understanding whether or not there is a flavor dependence to the EMC effect. It is essential to understand the ultimate sensitivity of various experimental approaches, including realistic systematic and model-dependent uncertainties.

We have updated the discussion of both the experimental uncertainties and the model-dependent corrections required to interpret the results in terms of the flavor dependence, presented in Sec. 6.2. We have performed extensive sensitivity studies using these updated uncertainties, and compare our projected results to a range of estimates for the size of the flavor dependence in Sec. 4.3. This includes some extreme models considered in other proposals to simplify comparison of the overall sensitivity of the different approaches. We also directly evaluate the sensitivity of the inclusive ^{48}Ca/^{40}Ca ratios, both for the measurement as approved and assuming a four-fold increase in statistics, yielding a systematics-dominated measurement. These are summarized below and presented in detail in Sec. 4.4, along with comments on other experimental approaches aimed at studying the flavor dependence of the EMC effect.

PVEMC:
Figure 2 shows the projected results for the proposed parity-violating measurement along with predictions from several models that yield a flavor-dependent EMC effect (Sec. 4.2). To show the importance of the normalization uncertainties, the projected data points for the right hand figure are shifted towards the
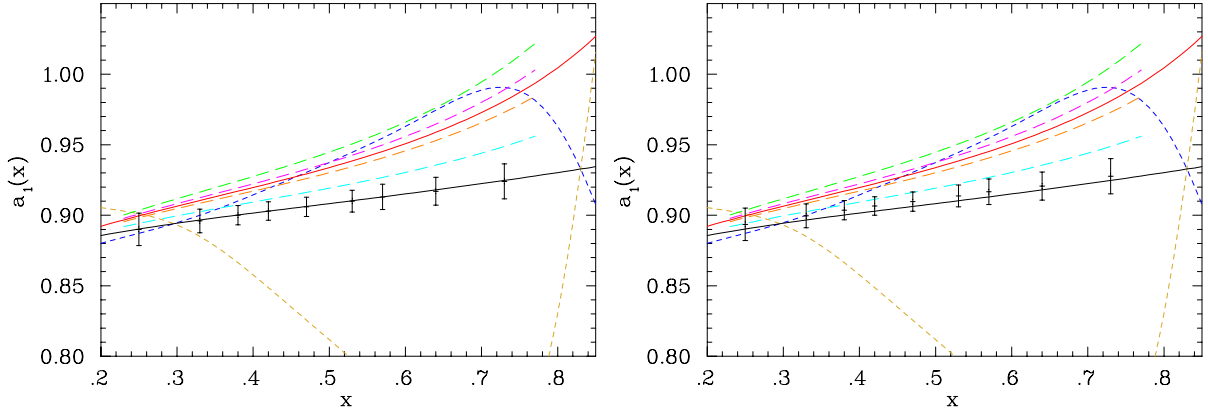
Figure 2: Projected uncertainties for PVEMC along with various model predictions that include flavor-dependent EMC effect contributions. The solid black line is the prediction of the SLAC E139 (flavor-independent) fit, the solid red line is the prediction of the CBT model (Sec. 4.2.1), the long-dashed lines (green, magenta, orange, cyan) are predictions based on simple models of the underlying physics described in Sec. 4.2.3, and the short-dashed blue and yellow lines represent extreme cases where the entire EMC effect comes from modification of only up (or down) quarks. In the left panel, the projected data points are placed on the flavor-independent curve, while the right panel shows the impact of a one-sigma normalization shift.

CBT curve by the 0.4% normalization uncertainty. The precision of the proposed measurements is sufficient to make meaningful measurements for even the smallest of the flavor-dependent signals from the models evaluated here, and provides a $\sim 8\sigma$ sensitivity to the CBT model (red line), neglecting the normalization uncertainty, $\sim 7\sigma$ if the data is shifted by the 0.4% normalization uncertainty.

^{48}Ca/^{40}Ca **cross section ratios:**
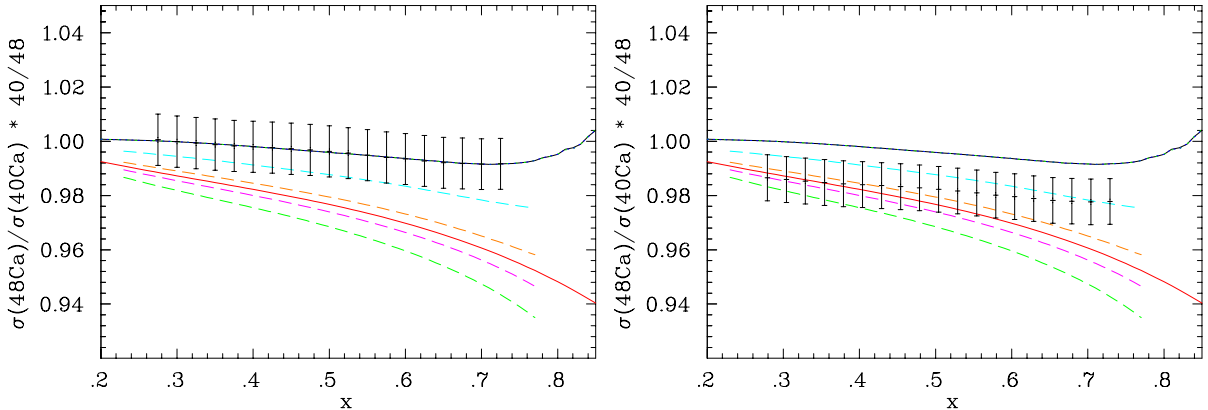
Figure 3: Projected uncertainties for the upcoming E12-10-008 ^{48}Ca/^{40}Ca ratios (bottom) [13] **under the assumption that the cross section ratios are taken with four times the proposed statistics**. The curves are the same models as shown in Fig. 2. In the left panel, the projected data points are placed on the flavor-independent curve, while the right panel shows the impact of a one-sigma normalization shift.

Figure 3 shows the projected uncertainties for the inclusive ^{48}Ca/^{40}Ca ratio of the cross section per nucleon [13] based on increased statistical precision over [13] (Sec. 4.4.1). To show the importance of the normalization uncertainties, the projected data points for the right hand figures are generated assuming a flavor-independent EMC effect but shifted towards the CBT curve by the 1.4% normalization uncertainty.

It is clear from the right-hand figure that the small signal from flavor-dependent predictions, combined with the large normalization uncertainty, make it difficult to cleanly observe even a relatively large flavor dependence. An analysis of the slope, which is insensitive to normalization uncertainties, provides a 2.3σ after accounting for the $\sim$10% loss of sensitivity due to the model dependence of the isoscalar correction, as described in Sec. 4.4.1.

SIDIS in ^{3}H and ^{3}He:

We do not provide a quantitative comparison for the conditionally approved SIDIS measurement in ^{3}H and ^{3}He [14], as we don't have sufficient information on the expected systematic uncertainties. However, as presented in Sec. 4.4.2, there is minimal sensitivity except for perhaps the most extreme models, and even these typically yield effects at the 3-5% level on the sensitive observables. In addition, we note that the systematic uncertainties will have a larger impact on observables that involve differences between π^+ and π^- cross sections, or differences between ^{3}H and ^{3}He cross sections, when these differences are small.

Pionic Drell-Yan:

The AMBER collaboration will make measurements of pionic Drell-Yan from heavy nuclei and deuterium, which is sensitive to the ratio of nuclear quark pdfs. A more detailed discussion is presented in Sec. 4.4.3, but the kinematic coverage of the measurement is limited to $x \leq 0.34$. This will provide complementary information in the lower-x region, but has minimal overlap with the EMC region and the kinematics of the proposed PVEMC measurements.

Conclusions:

	PVEMC (this proposal)	^{48}Ca/^{40}Ca ratios E12-10-008
Uncertainties		
Statistics	0.7-1.3%	0.5% (0.95%)
Systematics	0.5-0.7%	0.7%
Normalization	0.4%	1.4%
Projected Sensitivity (CBT model)		
Neglecting norm. uncertainty	7.9σ	2.9σ (2.1σ as proposed)
Applying a 1σ norm. shift	7.1σ	2.3σ (1.7σ as proposed)
Applying a 2σ norm. shift	6.6σ	2.3σ (1.7σ as proposed)

Table 1: Projected uncertainties and significance of the deviation from the flavor-independent EMC effect (null-hypothesis) for pseudo data generated following the CBT model [1, 15]. Also illustrated is the sensitivity if we apply a normalization shift to move the data towards the null hypothesis.

Table 1 shows the projected uncertainties and the sensitivity of PVEMC and the calcium cross section ratios to the prediction of the CBT model. The first result is based on the chi-squared comparison between the projected data (generated according to CBT) and the flavor-independent curve, neglecting the normalization uncertainty. The other entries show the sensitivity if the data is generated according to the CBT model but with a 1σ or 2σ shift of the normalization. The proposed parity violating measurement yields a 7.1σ sensitivity after applying a 1σ normalization shift, and 6.6σ sensitivity with a 2σ shift in the normal-

ization. We take this as a lower limit of the likely sensitivity as it is based on arbitrarily shifting the data to minimize the signal. **Not only is the measurement sensitive to the CBT model at the 6.6σ or better, it is also sufficient to provide 3σ evidence for all but the smallest effects shown in Fig. 2 (and $>2.5\sigma$ for even the smallest model), and a significant ability to discriminate between models with a "large" flavor dependence from models yielding smaller effects.** Thus, the measurement has significant discovery potential and, if flavor dependence is observed, will provide a quantitatively significant measurement of the size of the effect that will help understand the origin of the EMC effect and constrain the impact of the flavor dependence on other high-energy observables on non-isoscalar nuclei.

The ^{48}Ca/^{40}Ca inclusive cross section ratio, even with the assumed increase in statistical precision, provides very limited sensitivity to flavor dependence. A result consistent with the flavor-independent prediction would provide minimal constraints on flavor dependence, excluding only the most extreme prediction at the 3σ level. **If the data end up being in perfect agreement with the CBT model, it would only provide a $\sim 2.3\sigma$ signal for flavor dependence, not meeting the 3σ criteria for evidence. It would also be consistent with all or other models at the 1-1.5σ level or below**, as illustrated in Fig. 4.
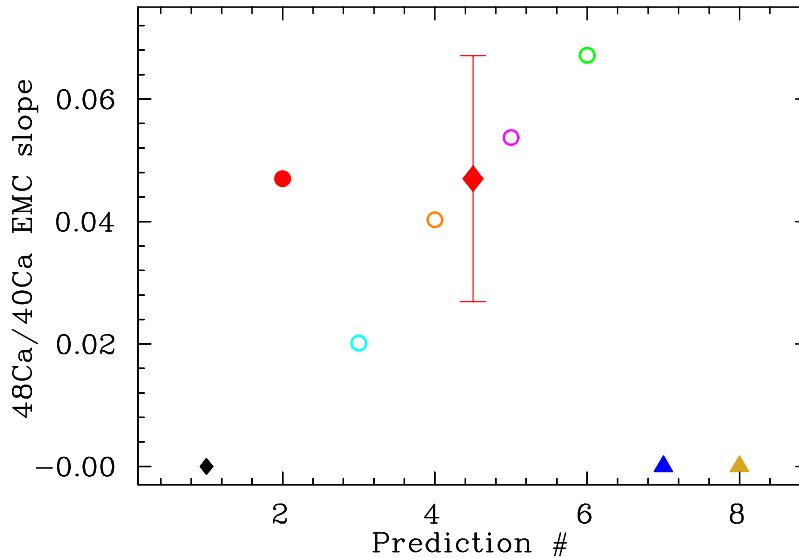
Figure 4: Projected measurement of the ^{48}Ca/^{40}Ca slope for the E12-10-008 measurement with a four-fold increase in statistics, assuming the data match the CBT model. The slope is after applying the isoscalar corrections and scaling from A=40 to A=48 based on the E139 fit. The predictions are for the E139 flavor-independent parameterization (1), CBT model (2), Scaling models (3-6), and up-(down-)quark only EMC effect (7,8).

Based on our examination of various proposed techniques to study the flavor-dependent EMC effect (Sec. 4.4), we believe that no other measurement currently planned or under discussion can provide the sensitivity proposed by this measurement. As such, we believe that the PVEMC experiment will be a critical step in identifying and quantifying flavor dependence of the EMC effect, and should be performed no matter what is observed in the ^{48}Ca/^{40}Ca ratios.

3 Introduction

Within QCD we describe the structure of protons and neutrons in terms of their underlying quark and gluon degrees of freedom. Protons and neutrons are also the basic building blocks of more complex systems (nuclei) and this transition between QCD and nuclear physics is still out of reach for modern theory. The effective theories we have for the description of inter-nucleon interactions have been widely successful in producing detailed descriptions of systems such as nuclear structure and scattering processes. However, they are based around the concept that nucleons in the nuclear environment strongly maintain their identities and have few, if any, provisions for how they change.

An open and important question for hadronic physics today is how protons and neutrons are modified when they are bound in a nucleus and how one makes the transition between traditional nuclear physics to QCD. The observation of the "EMC effect", the depletion of the nuclear quark distributions for $0.3 < x < 0.8$ relative to the expectation from nucleon pdfs plus Fermi motion, provides clear evidence that the nuclear pdfs are not simply the sum of the pdfs of unmodified proton and neutrons [16, 17, 18]. But despite this direct measurement of such modification, the underlying physics mechanism(s) for it is not well understood.

While the existence of nuclear modification of the pdfs is well established, important questions remain about the nature of the modification: a detailed description of its A dependence is not yet complete, and we have almost no experimental information on the spin- and flavor-dependence. An improved understanding of these questions will be enormously important in guiding a theoretical understanding, but it is also a pressing experimental issue with broad implications. Without an understanding of the behavior in light nuclei, we rely on models of the modification in the deuteron and ^{3}He in extracting free neutron structure from "effectively free" neutrons in these light nuclei. With no understanding of the flavor dependence, electron- and neutrino-nucleus scattering and nucleus-nucleus collisions assume flavor-independent modification to the pdfs. In electron-nucleus scattering, neglecting potential flavor dependence can impact studies of the A dependence for non-isoscalar nuclei, and yield unknown corrections to DIS and SIDIS measurements from polarized ^{3}He targets. It can have similar impact on neutrino-nucleus scattering, Drell-Yan measurements, high-energy nucleus-nucleus collisions, and for future EIC measurements.

The flavor dependence of the EMC effect has received a great deal of attention in recent years [19, 20, 3, 5, 6], with calculations that examine the flavor and spin dependence of the EMC effect, including some which indicate significant flavor dependence in non-isoscalar nuclei [1, 15]. In addition, the observation of the correlation between the EMC effect and short-range correlations (SRCs) [21, 22, 11, 23] combined with the known isospin structure of SRCs [24, 23] suggest an alternative mechanism for generating such a flavor dependence. While there are now many reasons to believe that the EMC effect should differ for up- and down-quarks in non-isoscalar nuclei, there is essentially no experimental evidence that supports this hypothesis. As such, it is critical to have a measurement that can cleanly isolate the flavor dependence of the EMC effect, independent of other nuclear effects, and with the precision to quantify the flavor dependence as input to parameterization of the EMC effect and to guide detailed calculations of the underlying physics.

One of the primary goals of Jefferson Lab is to study nuclear modification and to study how one can relate the basic QCD degrees of freedom, quarks and gluons, to the objects that nature most readily presents to us, nucleons and nuclei, through the use of the well-understood electron probes. With the 12 GeV upgrade, we will have unprecedented access to the valence quark kinematic region allowing for new constraints on modification. By far, most of the data available on parton distributions is through electromagnetic scattering, which is heavily weighted to the the u-quark distributions and is only sensitive to one particular linear combination of quarks. Parity-violating deep inelastic scattering with leptonic probes provides a powerful method to access *flavor ratios* of quark distributions that have not been as well explored and offers opportunities to study difficult-to-obtain flavor dependent effects within nuclear modification.

The scattering cross section for weak neutral currents is dependent on both the amplitudes for the ex-

changed virtual photon and neutral Z boson, which interfere to give

$$\sigma \propto |A_\gamma + A_Z|^2 \,. \tag{1}$$

For $Q^2 \ll M_Z$, the dominant term for the scattering rates is $|A_\gamma|^2$ and for the parity-violating component, the interference term $|A_\gamma^* A_Z|$. One can then form a parity-violating quantity which is the ratio of these two terms, and is measured by the differences between left and right-handed polarized lepton cross sections

$$A_{\mathrm{PV}} = \frac{\sigma_R - \sigma_L}{\sigma_R + \sigma_L} \sim \frac{|A_\gamma^* A_Z|}{|A_\gamma|^2}. \tag{2}$$

This asymmetry provides a particularly sensitive method to obtain flavor-dependent effects in nuclear modification as it is a ratio of the weak-to-electromagnetic interactions, which gives access to ratios of quark distributions.

3.1 Deep Inelastic Scattering and PDFs from Electromagnetic and Electroweak scattering

Deep inelastic scattering has provided one of the most important tools in understanding modern hadronic structure. From studying this scattering process we have some of our best evidence for the concepts of quarks as strongly interacting, point-like spin-1/2 objects, the running of the strong coupling constant α_s, and the validity of perturbative QCD, and confinement. It has been used for decades as a tool to map nucleon structure through parton distribution functions (PDFs) for which we have no predictions from first principles. The universality of these parton distribution functions is absolutely critical in our modern studies of deep inelastic neutrino scattering and of high-energy physics at facilities like the RHIC and the Large Hadron Collider.

At sufficiently large momentum and energy transfer from an electromagnetic probe to a hadronic target, a transition takes place where the underlying QCD degrees of freedom are exposed and the target appears as an incoherent sum of weakly interacting partons which we identify as quarks. The differential cross section for the electromagnetic scattering interaction can be written in the lab frame as

$$\frac{d^2\sigma}{d\Omega dE'} = \frac{4\alpha E'^2}{Q^4} \cos^2\frac{\theta}{2} \left[\frac{F_2(x, Q^2)}{\nu} + \frac{2F_1(x, Q^2)}{M} \tan^2\frac{\theta}{2} \right] \tag{3}$$

where α is the fine structure constant, Q^2 is the negative of the four-momentum transfer, E and E' are the initial and final probe energies, $\nu = E - E'$, M is the nucleon mass, and F_1 and F_2 are the quark-parton structure functions with x, the Björken scaling variable,

$$x = \frac{Q^2}{2M\nu}, \tag{4}$$

F_2 is expressed in terms of the quark and anti-quark parton distribution functions

$$F_2(x, Q^2) = x \sum_q e_q^2 \left[q(x, Q^2) + \bar{q}(x, Q^2) \right], \tag{5}$$

where e_q are the quark charges. This scaling variable has the interpretation of the fraction of momentum carried by that quark when the nucleon is boosted to the speed of light. The parton distribution functions $q(x, Q^2)$ carry the soft, non-perturbative nucleon structure and represent the probability that the quark carries that fraction of momentum x. The Q^2 dependence is predominantly logarithmic which is successfully predicted within the framework of perturbative QCD where it is order-by-order identified with phenomena such as soft gluon emission. Related to F_2 is F_1 through the longitudinal structure function $F_L = F_2 - 2xF_1$.

Equating $F_L = 0$ is the Callan-Gross relation and represents treating the partons as free, point-like spin-1/2 objects.

One challenge in this framework is accessing the quark flavor since the interaction is only sensitive to the charge-squared-weighted sum of the parton distributions, and therefore most heavily to the u-quarks. Exploiting charge symmetry between protons and neutrons, the idea that the u and d-quark distributions are symmetric between the two, and suppressing the sea quark contributions through studies at high x, a deconvolution can be performed. However, since there are no sufficiently high luminosity free neutron targets, neutrons are typically studied bound in a nucleus such as deuterium. How representative such a target is to the free neutron beyond simple binding effects is an open question, but deuterium measurements remain a standard in extracting neutron physics.

A method of accessing quark flavor information without having to consider such binding effects is through parity-violating processes which measure weak force couplings to the quarks. For now we assume the Callan-Gross relation and $Q^2 \gg M^2 x^2$; the full framework is presented in Appendix A. In the quark-parton model, the left-right polarized lepton scattering asymmetry given in Eq. 2 can be expressed in terms of the parton distribution functions by

$$\frac{\sigma_R - \sigma_L}{\sigma_R + \sigma_L} = A_{\text{PV}} = -\frac{G_F Q^2}{4\sqrt{2}\pi\alpha} \left[Y_1 a_1(x) + Y_3(y) a_3(x) \right], \tag{6}$$

where G_F is the Fermi constant and

$$Y_1 \approx 1 \ ; \ \ Y_3(y) \approx \frac{1 - (1-y)^2}{1 + (1-y)^2} \tag{7}$$

with

$$a_1(x) = g_A^e \frac{F_1^{\gamma Z}}{F_1^\gamma} = 2\frac{\sum_i C_{1i} e_i (q_i + \bar{q}_i)}{\sum_i e_i^2 (q_i + \bar{q}_i)} \ ; \ \ a_3(x) = g_V^e \frac{F_3^{\gamma Z}}{2F_1^\gamma} = 2\frac{\sum_i C_{2i} e_i (q_i - \bar{q}_i)}{\sum_i e_i^2 (q_i + \bar{q}_i)}. \tag{8}$$

with $y = \nu/E$, g_A^e and g_V^e the axial and vector couplings to the electron respectively, and C_{1i} and C_{2i} the effective quark couplings dependent on the weak-mixing angle $\sin^2 \theta_W$. In practice the a_1 term dominates the asymmetry as the C_{2i} couplings are suppressed by an order of magnitude relative to C_{1i}.

The power of this method is elucidated when one considers nuclear quark distributions for the light flavors u_A and d_A and expand a_1 about the isoscalar $u_A = d_A$ limit and at high enough x where the sea quarks do not contribute significantly

$$a_1 \simeq \frac{9}{5} - 4\sin^2 \theta_W - \frac{12}{25} \frac{u_A^+ - d_A^+}{u_A^+ + d_A^+} \tag{9}$$

with the convention that $q^\pm = q(x) \pm \bar{q}(x)$. Parity-violating deep inelastic asymmetry measurements are therefore directly sensitive to differences in the quark flavors. In turn, for isoscalar targets (and neglecting sea quarks) a_1 roughly becomes a constant and the measurement becomes a test for charge symmetry violation [25].

3.2 Nuclear PDF Modification and the EMC effect

The EMC effect, first reported by the European Muon Collaboration collaboration [26] almost 40 years ago, provided the first direct evidence that the quark distributions in nucleons bound in a nucleus are significantly different from those of free nucleons. This was demonstrated by observing a difference in the ratios of deep-inelastic muon scattering cross sections between a heavy nucleus (in this case iron) and deuterium. They

showed that this ratio deviated from a simple constant expectation across a range of x, as confirmed for a range of nuclei at SLAC [27] and JLab [21], as shown in Fig. 5. To compare between nuclei where $N \neq Z$, a model-dependent "isoscalar" correction is made to the interaction cross section to account for an excess of neutrons, typically assuming that the free nucleon structure functions can be used to correct for presence of excess neutrons in nuclei.
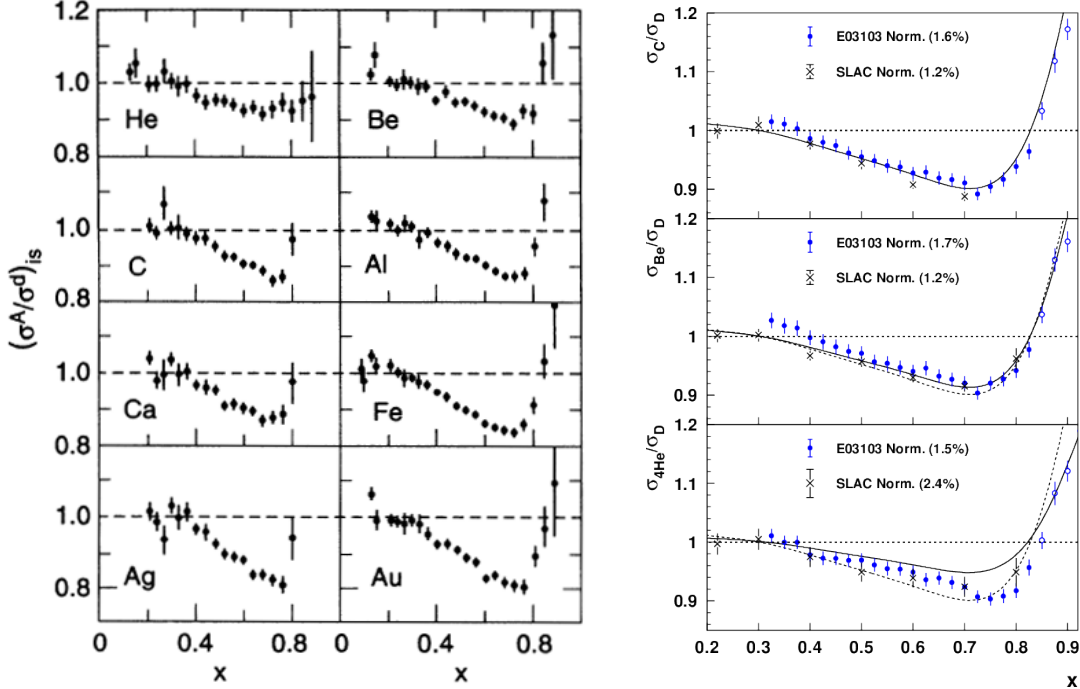

Figure 5: Data demonstrating the EMC effect for a range of nuclei from SLAC E139 [27] (left plot) and JLab E03-013 [21] (right plot).

Prior to JLab experiments, the large-x EMC ratios, $(\sigma_A/A)/(\sigma_D/D)$, where σ_A has been corrected for neutron excess, for various nuclei showed the following features,

- an enhancement attributed to Fermi motion for $x > 0.9$,

- a suppression in the range $0.3 < x < 0.8$, dubbed the "EMC effect", with a minimum around $x = 0.7$

- a universal x dependence in the EMC region, with the size of the suppression slowly increasing with A (scaling as the average nuclear density)

Fermi motion gives a strong enhancement to the nuclear structure function for $x > 0.8$ due to the enhanced impact of smearing caused by nucleon motion at large x, where the nucleon pdfs are going rapidly to zero. We focus here on the "EMC region", generally taken to be $0.3 < x < 0.7$. Shortly after the data was obtained, it became clear that Fermi motion alone was insufficient to explain the effect. Despite decades of work there is still no commonly-accepted explanation for the EMC effect; we refer the reader to the following reviews [16, 17, 18].

In the last decade or so, Jefferson Lab has provided important new data that has modified our understanding of the EMC effect. First, measurements of the EMC effect in light nuclei [21] demonstrated that the EMC effect does simply scale with nuclear density, as ^9Be shows roughly the same EMC effect as ^4He

and ^{12}C, despite having an extremely low average nuclear density. It was initially suggested that this surprising result was related to the significant cluster structure in ^{9}Be, which has a significant component with two alpha particles and an extra neutron. While the average nuclear density is low, most of the nucleons (and all of the protons) are in dense, alpha-like clusters, and so their local environment is a dense cluster.

A short time later, the same nuclear dependence was observed in the contribution of Short-Range Correlations (SRCs) in light nuclei [22], with ^{9}Be having a greater contribution from SRCs than expected based on conventional models where the contribution scaled with the nuclear density. SRCs are pairs of nucleons with large relative momentum generated by interaction via the strong short-range components of the NN interaction. As such, it was natural that the contribution of SRCs would relate to the number of nucleons that are extremely close together, and therefore also be enhanced due to the strong alpha clustering in ^{9}Be. In this 'local density' picture initially used to describe the EMC ratios for light nuclei, both the the EMC effect and presence of SRCs are the result of configurations with nucleons very close together. However, the correlation between the observed EMC effect and number of SRCs for various light and heavy nuclei also suggested another possibility [28], that the EMC effect was directly generated by the presence of the high-momentum pairs of nucleons in the SRC, with the nucleon modification driven by large off-shell effects in these highly-virtual configurations. Because of the isospin structure of SRCs, which are strongly dominated by np pairs [29, 30, 31, 23], minority nucleons will spend a larger fraction of their time at extremely large momenta, which would translate to an enhanced EMC effect for these nucleons in a picture where the EMC effect is driven by off-shell effects. **It is interesting to note that recent calculations that include a flavor dependence to the EMC effect [1, 15], and a range of scaling models based on the idea of the EMC effect being driven by local density or high virtuality [3] all predict that the EMC effect is enhanced in the minority nucleons, although the predicted size of the isospin dependence varies significantly.**

Historically, explanations of the EMC effect have neglected the potential impact of flavor-dependent effects, and many have neglected the impact of detailed nuclear structure, focusing on effects which have simple scaling behavior with nuclear mass or density [27, 16, 17]. **Recent measurements of the EMC effect in light nuclei [21, 20] have made it clear that a complete understanding of nuclear PDFs requires a detailed understanding of the connection between the nuclear effects and details of the nuclear structure. It is also clear that our understanding of the EMC effect will not be complete without an understanding of the flavor-dependence of the nuclear modification to PDFs.** As noted above, the data for heavier nuclei show a slow increase in the nuclear modification as A increases, but these nuclei have $N > Z$, and are thus sensitive to both the overall A dependence and any flavor-dependent effects. Because there is a strong correlation between A and N/Z for heavier nuclei, it is difficult to disentangle A-dependent effects from any flavor dependence without additional theoretical or experimental guidance. The Particle Data Group states in their 2013 review of the electroweak model that *"it would be important to verify and quantify this kind of effect experimentally, e.g., in polarized electron scattering."* [32]

While a flavor-dependent effect is challenging to study in conventional measurements of the EMC effect, as discussed in Sec. 4.4.1, the flavor sensitivity of parity-violating electron scattering provides an ideal probe of such effects. The parity-violating asymmetry in deep inelastic scattering provides direct access to flavor dependence in the EMC effect, cleanly separated from flavor-independent nuclear modification of the PDFs.

3.3 Possible Indications of Flavor Dependence

Most models and parameterizations of nuclear PDFs do not include flavor-dependent medium modification, and so any true flavor dependence in neutron-rich nuclei is absorbed into the parameterization of the A dependence. This can have an important impact on any measurement where the flavor sensitivity differs from direct measurements of the nuclear PDFs. Measurements involving weak coupling to the nuclear quark distributions will have a different contribution from up and down quarks, and a flavor-independent modification of the nucleon PDFs will not yield the correct result. Similarly, nuclei with unusual N/Z ratios

will not be well represented by conventional parameterizations of the EMC effect. For most nuclei, the A-dependent parameterizations of the EMC effect will be fairly reliable, as nuclei in a given mass region tend to have a relatively narrow range of N/Z values. However, a difference between the EMC effect for up-quark and down-quark distributions could change the nuclear effects in ^{3}H or ^{48}Ca from those observed in ^{3}He or ^{40}Ca.

In light of the importance of such an effect, several avenues should be explored and by using data from multiple techniques, a more complete picture can emerge. While we discuss several possibilities, we stress that the parity-violating technique presented here offers one of the most direct, precise, and theoretically clean ways to access these observables and would serve as the strong underlying foundation for all of these studies. In this section, we present observables that are sensitive to a flavor dependent EMC effect, and have been discussed as potential signatures for such an effect. However, while these observables are clearly impacted by flavor dependence, none of them provide clear or direct evidence for a flavor dependent EMC effect.

3.3.1 The "NuTeV Anomoly"

The NuTeV experiment [33] at Fermilab was designed as a measurement of the electroweak mixing angle $\sin^2 \theta_W$ through neutrino deep inelastic scattering measuring together charged and neutral current neutrino and anti-neutrino scattering. With those cross sections, one can measure the weak mixing angle using the Pachos-Wolfenstein relation [34],

$$R_{\text{PW}} \equiv \frac{\sigma(\nu_\mu N \to \nu_\mu X) - \sigma(\bar{\nu}_\mu N \to \bar{\nu}_\mu X)}{\sigma(\nu_\mu N \to \mu^- X) - \sigma(\bar{\nu}_\mu N \to \mu^+ X)}. \tag{10}$$

which reduces to $\frac{1}{2} - \sin^2 \theta_W$ in the case of an isoscalar target and the absence of charge symmetry violation. This quantity is particularly attractive to study as a large number of systematic uncertainties cancel, including a great deal of nuclear structure. However, important corrections must be made in the case where there is an excess of neutrons which is the case for heavy nuclei typically used as targets in neutrino experiments.

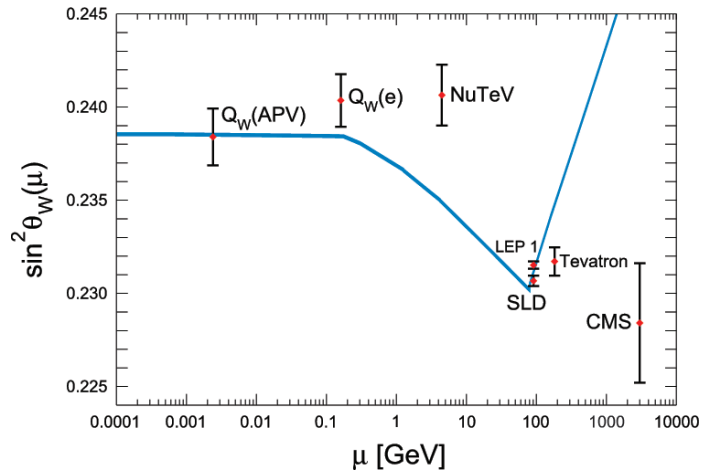Figure 6: Constraining world data on the running of $\sin^2 \theta_W$ including the published NuTeV result [33].

For NuTeV, high purity ν and $\bar{\nu}$ beams from the decay of charged pions or kaons were produced by the Tevatron and the neutrino interactions were detected 1.5 km downstream in a large detector array. This array consisted of steel-scintillator target calorimeter followed by an iron-toroid spectrometer. The pub-

lished result on $\sin^2\theta_W$ was approximately 3σ from the standard model prediction, Fig. 6 and has caused a significant amount of discussion in the community regarding the discrepancy [35].
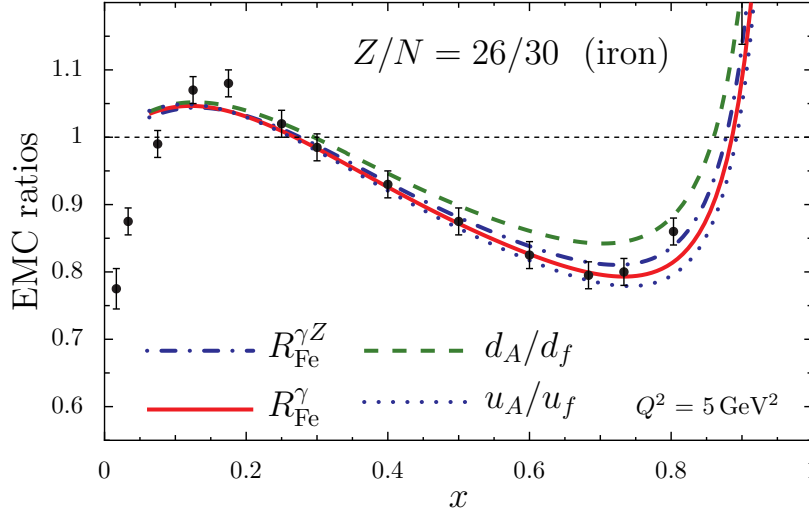

Figure 7: Isovector parton distribution modification in Fe from Cloët *et al.* [15]. The dashed and dotted lines show the modification for d and u quarks, respectively, and the solid and dashed lines show the ratio of nuclear pdfs to proton plus neutron in electron scattering and for the $\gamma - Z$ interference contribution.

A large class of possible explanations has been generated involving unconsidered corrections in the NuTeV analysis, including higher order QCD evolution, a strange sea asymmetry, charge symmetry violation, nuclear shadowing, or a flavor-dependent EMC effect. A calculation of the isovector EMC effect by Cloët *et al.* [1, 15], which we discuss in Sec. 4.2.1, is shown in Fig. 7. In this model, a flavor dependence modifies the nuclear u- and d-quarks differently within the iron nucleus, irrespective of the nucleon in which they are bound, by the mean isovector field from the surrounding nucleus. This model can account for 2/3 of the observed difference, resolving the discrepancy and leaving significantly less room for additional corrections.

While this demonstrates the importance of understanding the flavor structure of the target in the NuTeV measurement, the fact that many different ways to resolve the discrepancy have been proposed makes it difficult to treat this as a strong indication of a flavor-dependent EMC effect without additional data to support this particular explanation. At the same time, without quantification of the flavor dependence of the EMC effect, which must be there at some level, we do not have a quantitative understanding of what additional effects would be required to resolve the NuTeV anomaly.

3.3.2 The EMC-SRC connection

As noted in Sec. 3.2, the observed correlation between the EMC effect and the strength of Short-Range Correlations (SRCs) in nuclei led to the question of whether the isospin structure of SRCs, where minority nucleons are more likely to be part of an SRC, translates into an enhanced EMC effect for these minority nucleons [5, 23]. This typically assumed that the large-momenta associated with the SRCs is the source of the EMC effect through the off-shell corrections in these Highly Virtual (HV) configurations. In this case, the isospin structure of SRCs would drive a similar structure in the EMC effect. Another explanation for the similar behavior in the EMC effect and SRCs was based on the idea that the modification occurs within short-distance configurations (as opposed to high-momentum configurations), and the probability of nucleons being very close together drives both the EMC effect (through nucleon overlap) and the generation
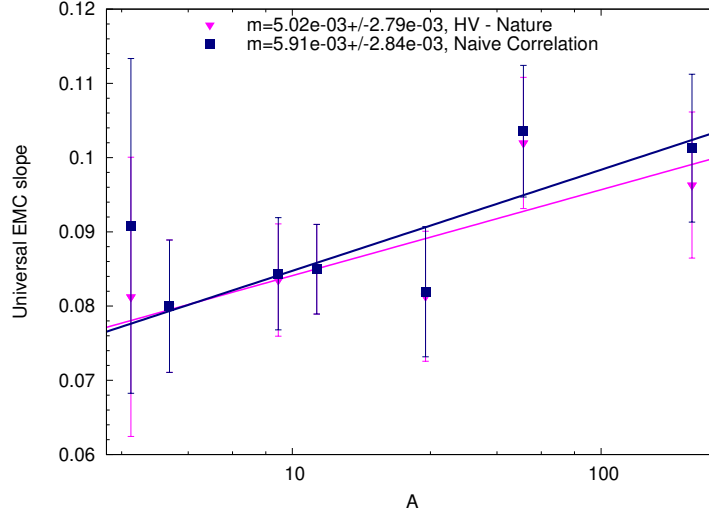
Figure 8: The slope of the "universal EMC effect" vs A, based on the analysis of Ref. [5] ("HV - Nature"), and the naive (flavor-independent) result where the EMC slope is scaled down by a factor of a_2, the relative SRC contribution in heavy nuclei compared to the deuteron.

of SRCs (associated with the short-distance part of the NN potential). In this case, both effects are driven by the local density (LD) as seen by the nucleons in the nucleus, which does not necessarily imply an isospin dependence in the EMC effect [20].

Examinations of the quality of scaling between the EMC effect and SRCs [11] slightly favor the flavor-independent LD hypothesis over the flavor-dependent HV model, but only at the 2σ level, and with some model dependence in the comparison. A more recent examination found that assuming the HV picture yielded a universal EMC effect per deuteron [5], consistent with the idea that the SRCs drive the EMC effect, but a later work [6] showed that the same was true under the flavor-independent LD assumption, and the LD picture again gives a somewhat better description of the data.

Existing measurements of the EMC effect in non-isoscalar nuclei have limited direct sensitivity to the flavor dependence of the EMC effect, as illustrated in Fig. 8. The figure shows the universal EMC slope from the HV approach of Ref. [5] ("HV-Nature") to that obtained from the most naive analysis of the correlation ("Naive Correlation"). In the naive correlation analysis, the EMC effect is assumed to scale with a_2 (the relative contribution of SRCs in the heavy nucleus compared to the deuteron), neglecting any isospin structure of the SRCs (and thus flavor-dependence in the EMC effect). The two models, one with explicit flavor dependence and one without, are identical for isoscalar nuclei and show only small differences for non-isoscalar nuclei, below 0.5σ for even the most neutron-rich nucleus (Au).

Because the impact of an explicit flavor dependence on the inclusive EMC effect is small, it is difficult to use such measurements to provide meaningful constraints. Section 4.4.1 includes a detailed evaluation of the sensitivity of a direct comparison of ^{48}Ca to ^{40}Ca and shows that such a comparison, while more sensitive than existing data, will not answer the question of whether or not there is a flavor dependence to the EMC effect.

3.3.3 PDF Fits

There have been several global analyses that have examined the possibility of flavor dependent nuclear effects. Primarily, these analyses have concentrated on the tension between data from neutrino interac-

tions (charged current) and data from charged lepton scattering and Drell-Yan (neutral current) in fits that assume a flavor-independent modification of the light quark distributions in nuclei. An analysis by Schienbein *et al.* [36, 37] noted a striking difference between the nuclear correction factors F_2^A/F_2^D found by fitting charged lepton (neutral current) and Drell-Yan data compared to fitting charged current neutrino scattering data, Fig. 9. In this method, comparisons between "free" nucleon PDFs to the nuclear PDFs are made. Later Kovarik *et al.* [38] performed a global analysis using partitions of the neutrino-nucleus DIS, charged lepton-nucleus DIS, and Drell-Yan data to test the compatibility between these data sets. In the Kovarik "nCTEQ" analysis, a goodness of fit test is used while varying the contribution weights between the set of neutral current (lepton and Drell-Yan) data and charged current the neutrino data. In those two partitions, they find no compromise fit that has acceptable χ^2/NDoF simultaneously for both sets at the 90% confidence level. Furthermore, individual data sets from the NuTeV neutrino iron results and from lepton-Fe exceed the 99% limit in the compromise fits.
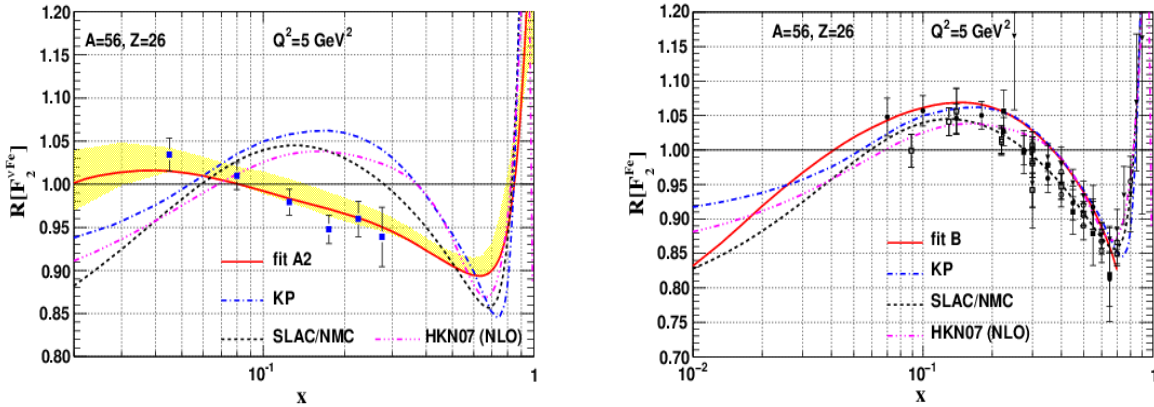

Figure 9: Differences in the nuclear correction factors $R = F_2^A/F_2^N$ for charged current neutrinos (left panel) and for neutral current leptons and Drell-Yan (right panel) evaluated at $Q^2 = 5\mathrm{GeV}^2$. Figures taken from Ref. [37].

This result contrasts one by de Florian *et al.* [39] which was a global fit where the nuclear effects are parameterized and included in the fit. In that analysis they claim compatible fits within their errors between all data and cites possible differences in the overall deuterium normalization (Kovarik calculates the deuterium from free PDFs, rather than use the sparse neutrino data) or possibly "disregarded uncertainties" and "theoretical ambiguities". While the de Florian analysis included neutral and charged pion production data from RHIC as well, the χ^2/dof for these additional data sets do not appear anonymously large. An analysis by Paukkunen *et al.* [40] notes that only the NuTeV neutrino data and data from CHORUS (lead), CDSHW (iron), and the NuTeV antineutrino data show no controversy. Later they argue [41] that unnoticed fluctuations in the overall normalization to the NuTeV data are sufficiently large to cause tension.

A review of these issues is given in Ref. [42], Section 8. There they suggest that when the full uncertainties for all the measurements are taken in quadrature, as in the de Florian fit, the discriminating power for tension may be reduced. The amount of controversy and uncertainty highlights the need for measurements such as this proposal which can unambiguously address the situation.

3.3.4 SIDIS

Semi-inclusive deep inelastic scattering provides access to quark flavor with an electromagnetic probe by tagging pions in the final state of the reaction. Such methods rely on factorization in which the hadronization process is decoupled from the initial parton distributions. A super-ratio of π^-/π^+ between deuterium and an asymmetric nuclear target would be sensitive to variations in the flavors after a correction for differences between π^+ and π^- hadron attenuation effects in the nuclear environment. Constraining all possible hadronic and electromagnetic effects as one goes to large A and Z to sufficient precision is the primary challenge. Uncertainties in nuclear effects (including Coulomb effects) for π^+ and π^- production, challenges in obtaining complete kinematic coverage, and the requirement for demonstration of independent fragmentation to high precision led to the deferral of a previous proposal to examine the flavor dependence of the EMC effect in SIDS from heavy nuclei [43].

Conditionally approved CLAS experiment C12-21-004 [14] plans to make such a measurement via the comparison of π^+ and π^- production in ^{3}H and ^{3}He. In this measurement, nuclear effects are smaller and the comparison of π^+/π^- production in ^{3}H and ^{3}He should cancel some systematic effects. However, while nuclear corrections should be smaller, the size of the EMC effect for $A = 3$ nuclei [22], a factor of 3-4 smaller than for heavy nuclei, will reduce the size of the expected signal and thus the sensitivity, thus requiring extremely good statistical and systematic uncertainties.
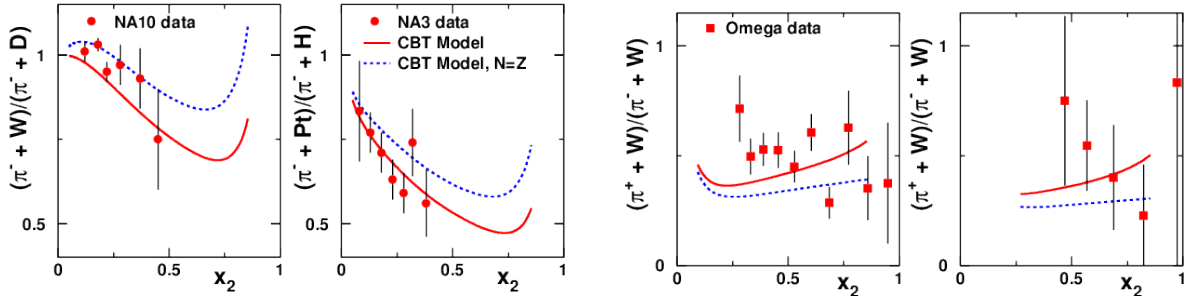
3.3.5 Drell-Yan

Figure 10: Existing pionic Drell-Yan data for ratios of heavy target to deuterium data compared to the CBT model [19]. A slight preference is shown for the CBT model, but is not conclusive. AMBER expects to be able to measure the Drell-Yan yield ratio $\sigma^{\pi^+W}/\sigma^{\pi^-W}$ with 5% statistical precision in the $0.08 \leq x_2 \leq 0.34$ range.

Drell-Yan measurements offer access to complementary data from DIS probes as they are sensitive to the flavors through the annihilation of sea quarks with the valence quarks of a heavy target. Proton Drell-Yan from nuclei from a fixed target is mainly sensitive to the proton valence and nuclear sea quark distribution, and so ratios of Drell-Yan from heavy nuclei to the deuteron providing sensitivity to the nuclear modification of the sea quarks. For pionic Drell-Yan, the pion quark distributions which are poorly constrained cancel in the ratio of $\sigma^{\pi^-A}/\sigma^{\pi^-D}$, providing access to valence quark distributions in nuclei. Because of the valence $\bar{u}$ in the π^- and the charged-squared weighting of the cross section, the π^- ratio is particularly sensitive to the u-quark EMC effect. Similarly, but without the benefit of the charge-squared weighting, the π^+ ratio shows sensitivity to the d-quark effects. As presented by Dutta *et al.* [19], within the CBT model there is a slight preference in existing pionic Drell-Yan measurements to support such an effect over the $N = Z$ predictions, but is not statistically strong, as can be seen in Fig. 10.

Future measurements will be performed by the AMBER collaboration at CERN, focusing on the low-x region, which will provide complementary information to the measurements proposed here. Further details on the projected results are provided in Sec. 4.4.3.

3.4 Impact of Flavor Dependent Nuclear Corrections on other measurements.

The observables presented in the previous section are sensitive to the presence of flavor dependence and were all, at least at one time, considered potential signatures of a flavor-dependent EMC effect. Without a clear understanding of the flavor dependence of the EMC effect, the interpretation of these data will be uncertain. We provide here additional examples of observables that will be modified in the presence of significant flavor dependent nuclear modification, but which, like the NuTeV anomaly, involve other corrections or uncertainties that are not sufficiently constrained to make these measurements useful as tests of the flavor dependence.

3.4.1 Neutron PDFs

The neutron structure function is often extracted from measurements on the deuteron, with significant corrections to account for the proton contribution, especially at large x values. The neutron can also be extracted from comparisons of ^{3}H and ^{3}He structure functions. In this case, only the difference of the nuclear corrections for these two nuclei enters into the extraction of F_{2n}, and this is directly sensitive to the difference in the nuclear effects for the proton and neutron. Even with the assumption that the proton distributions in ^{3}He are identical to the neutron distributions in ^{3}H, there is a difference in the relative nuclear effects when including only conventional smearing corrections [44]. While this portion of the isospin dependence (and its estimated uncertainty) is accounted for in calculations aimed at extracting F_{2n}/F_{2p} from the ratio of ^{3}He to ^{3}H, additional flavor dependence associated with nuclear effects beyond simple binding and Fermi motion will yield an additional correction. While the main MARATHON analysis [45] assumes that any flavor dependence beyond what is included in the Kulagin and Petti model [46, 47] is negligible, other approaches [48, 10] raise questions about this assumption.

Polarized ^{3}He nuclei are often used as effective polarized neutron targets. The use of such targets in DIS and SIDIS measurements will be sensitive to the flavor dependence of nuclear effects in both the polarized and unpolarized pdfs. As noted above, some models account for the isospin dependence associated with the difference in proton and neutron distributions in the nucleus, but neglect any flavor dependence beyond this.

We note that while the ^{3}H/^{3}He ratio is sensitive to both F_{2n}/F_{2p} and the flavor dependence of the EMC effect, the current level of uncertainty on F_{2n}/F_{2p} is such that the data cannot be used as a direct measure of the flavor dependence of the EMC effect. Other experiments can also provide model-independent extractions of the neutron structure function, but this will not allow a comparison of the nuclear effects unless the precision is significantly better than the extraction from MARATHON. More specifically, the total uncertainty in the neutron extraction must be smaller than the model-dependent contribution to MARATHON's extraction before limits can be set beyond the assumed upper limits taken in MARATHON's extraction of F_{2n}/F_{2p}. The difference between the models of the nuclear effects evaluated for the MARATHON experiment and in the flavor-dependent EMC effect based on np-dominance (maximal flavor dependence) is ~1% at large x, while the experimental uncertainties in this region are ~1.5%, so even with perfect knowledge of the neutron structure, MARATHON will have no meaningful sensitivity to the flavor dependence. This is not too surprising, as while the difference in N/Z for the nuclei is large, the total EMC effect is very small for A=3 nuclei. The MARATHON data has been included in global pdf fits to try and constrain the flavor-dependent effects, but the results provide limited evidence and are very sensitive to the assumptions made in the analysis [10, 49].

3.4.2 Nuclear Dependence of the EMC Effect

Measurements of the EMC effect in medium-to-heavy nuclei show that the effect scales approximately as the nuclear density, but the variation is slow and not precisely measured. Above mass 40, all measurements are made on neutron-rich nuclei, with N/Z generally increasing as one goes to heavier nuclei. As such, the observed A dependence of the EMC effect in heavy nuclei represents a combination of the density dependence and the neutron excess, meaning that even a modest flavor dependence could have a noticeable impact on the density dependence extracted when neglecting possible flavor-dependent effects. While nuclei like Au and Pb have a very large neutron excess and, potentially, a significant flavor dependence, they cannot be compared to isoscalar nuclei of similar mass, only nuclei of similar mass with somewhat different neutron excess. This makes the extraction of the nuclear dependence in heavy nuclei unreliable, and reduces their impact on constraining models of the EMC effect and on extrapolation of nuclear effects to symmetric nuclear matter.

3.5 Summary

The EMC effect is one of the best indications we have for the medium modification of bound nucleons and has been known for nearly 40 years, but the mechanism is still not understood. Experimentally, there is considerable room for additional investigation, in particular in the realms of asymmetric nuclei and small flavor differences in the modified quark distributions. Detailed calculations for the EMC effect as well as predictions based on simple assumptions about the underlying physics (e.g. that the EMC effect is driven by density, separation energy, or nucleon virtuality) all contradict the standard assumption that quark modification is entirely isoscalar. As such, it is hard to see how the EMC effect could be isospin independent, and parity-violating measurements offer out best opportunity to verify that the EMC effect is not flavor independent and to quantify the effect well enough to have real power to discriminate between models. Interestingly enough, all of these approaches predict an enhanced EMC effect for protons in neutron-rich nuclei, although the size of the effects predicted vary by a factor of three, as illustrated in the next chapter.

4 Measurements of the Flavor Dependence of the EMC effect

4.1 Choice of Target

To examine the hypothesis that there is a significant flavor dependence in non-isoscalar nuclei, it is clear that a large proton-neutron asymmetry is favorable. An isoscalar target would test for charge symmetry violating terms which are expected to be subdominant to an isovector effect. The SoLID PVDIS measurement on the deuteron will test charge symmetry violation through the same technique and will provide precision on the order of 1% up to $x = 0.7$ [50]. If the effects in deuterium turn out to be surprisingly large, an isoscalar measurement on a medium-to-heavy symmetric nucleus such as ^{40}Ca would likely be well motivated. Otherwise, the measurement is optimized by focusing on the non-isoscalar target.

There are many potential target options with sufficient neutron excess, though very high Z targets present additional complications which must be carefully considered. Our nucleus criteria include

- providing a high fractional neutron excess, $(N - Z)/A$, and relatively large EMC effect;

- minimizing radiative corrections and beam radiation which scale as Z^2 while scattering rates only scale with A;

- the size of Coulomb corrections and their impact on the parity-violating asymmetry.

A wide range of nuclei are possible candidates with reasonable values of $(N - Z)/A$ as well as a relatively large EMC effect. ^{9}Be, ^{48}Ca, and ^{208}Pb have $(N - Z)/A$ values of 0.11, 0.17, and 0.21, respectively. ^{9}Be would be expected to have a significantly smaller flavor asymmetry, as well as a somewhat smaller overall EMC effect, although a thicker target could be used. While the light nuclei may be of interest in testing microscopic calculations, such calculations do not yet exist and we focus on heavier nuclei, where the expected effect is larger.

For this experiment, we choose a target of ^{48}Ca due to its advantages over other heavier target. ^{48}Ca has a larger fractional neutron excess than other nuclei of similar mass, and as such is expected to have a larger flavor dependence, as seen in the CBT model [2] (Fig. 11) for which the flavor-dependent effect is half the size in ^{56}Fe compared to ^{48}Ca. For heavier nuclei like ^{208}Pb (or targets like depleted uranium and gold with similar N/Z), the flavor dependence scales roughly as N/A and so is $\sim$25% larger then for ^{48}Ca. While this would allow for an equivalent measurement with a factor of roughly 1.5 lower statistics, sufficient rates can be achieved with ^{48}Ca using only a 12% radiator, whereas an equivalent DIS rate in lead would require more than a 60% radiator (40% radiator for a longer run time or a measurement with reduced sensitivity). The radiative effects contribute non-linearly in the deconvolution scheme due to the rising cross section with lower-energy electrons having undergone radiation. It would also increase the photon and pion rates in the detectors and the radiation generated in the hall.

Coulomb corrections for high-Z targets have often been calculated in the so-called effective momentum approximation [51] and have been shown to be quite successful at lower energies even for targets as heavy as lead in quasielastic scattering [52]. In this approximation, the relative size of the correction is smaller as one goes to higher energy. For a heavy target like lead, a correction factor $V_C \approx 18$ MeV is applied to the incoming electron. V_C for ^{48}Ca is ~ 5 MeV and would have a sub-0.1% effect in this framework. The authors are unaware of calculations that have been carried through the full DWBA including the nuclear weak potentials for DIS.

4.2 Size of the Isovector EMC Effect

Quantitative predictions for the possible size of this effect are sparse, so we must rely on the few estimates available. However, we stress that this proposal is to provide a clean and sensitive measurement of

flavor-dependent nuclear effects in a sector where other potential measurements have limited sensitivity or significant model dependence, rather than to test specific models. Nonetheless, such models provide useful guidance in estimating the required precision for a significant experiment.

4.2.1 Cloët-Bentz-Thomas (CBT) model

It was proposed by Cloët *et al.* [1] that one possible resolution to the NuTeV anomaly was through the existence of an isovector EMC effect. Calculations, which we will call the Cloët-Bentz-Thomas (CBT) model, were carried out in the Nambu-Jona-Lasinio Model, which is a chiral effective theory treating the quark interactions as four-point contact interactions and contains important QCD concepts, such as confinement. To produce a nucleon model, the Faddeev equations are solved for a quark-diquark configuration. An isovector mean field is introduced and the free parameters are constrained to reproduce nucleon and nuclear properties such as nucleon masses and the empirical symmetry energy from the Bethe-Weizsäker formula. With these ingredients, quark distributions can be obtained for symmetric and antisymmetric matter.

This type of model has been very successful in reproducing the quark distributions for the EMC effect and the measured structure functions. In Ref. [1], the impact of the flavor-dependent nuclear PDF modification on the NuTeV anomaly was evaluated in the CBT model. The calculation was able to explain two-thirds of the anomaly, suggesting that the size of the flavor-dependent EMC effect predicted in this model is of the correct scale to resolve this long-standing issue.

Later predictions were made within this model specifically for the PVDIS a_1 term for iron and lead [15]. Calculations for ^{48}Ca were also provided for this proposal [53] and are shown in Fig. 11. The effect is qualitatively similar to lead, but slightly smaller due to the smaller neutron excess. The calculation shows a clear enhancement in a_1 over the isoscalar-corrected "naive" case that grows with increasing x. There is essentially no difference at $x = 0.2$, and a 5% difference at $x = 0.7$. We will be able to measure a_1 across this x range with a statistical precision that is typically below 1% and systematic uncertainties of 0.5-0.7%.
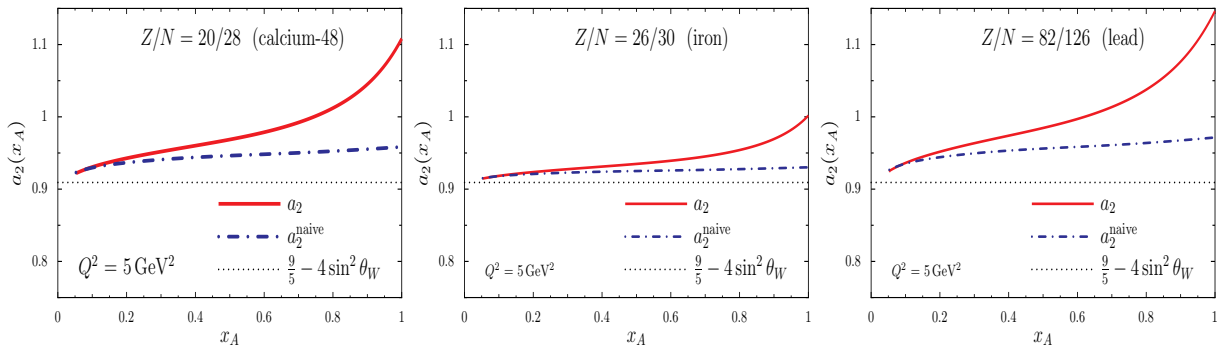

Figure 11: Predictions for a_2 for ^{48}Ca (left), iron (center), and lead(right) from [15, 53]. Note that the curves use a different convention and refer to a_2, which is the same as a_1 in our nomenclature.

4.2.2 Nuclear Parton Distributions

We consider data from PDF fits to understand present constraints in this sector and to consider the precision for new data required to become a significant test. First, we look at the nCTEQ nuclear PDF fits done by Refs. [37] and [38], discussed in Sec. 3.3.3. There the authors varied the contributions of neutrino charged current data with the standard DIS and Drell-Yan data. If there are flavor-dependent variations in the nuclear distributions, the discrepancy between the two in those fits provides an idea on their size.

The results of the a_1 calculations from this fit are shown in Fig. 12. The change in slope of a_1 of about 5% is consistent with the CBT calculation in the range of $0.2 < x < 0.7$. The fits including any neutrino data have a very different behavior than the neutrino-free fit in terms of the modification. This suggests that there is a lack of constraint on the order of a few percent in the DIS/Drell-Yan data in this observable, which is perhaps not surprising considering the unique flavor sensitivity of neutrino scattering.
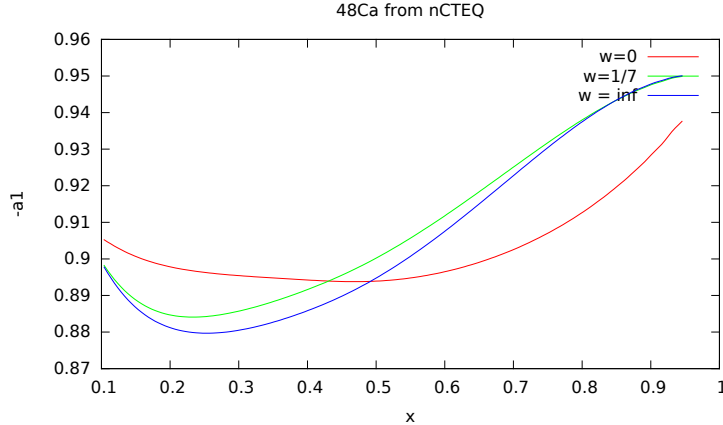

Figure 12: a_1 predictions from the nCTEQ data set assuming various weighting between pure DIS and Drell-Yan ($w = 0$) and pure neutrino data $w = \infty$ from Refs. [37] and [38] for ^{48}Ca. Inclusion of any fraction of neutrino data dramatically shifts the fit demonstrating the weakness of DIS data to this observable. The change in slope is about 5% over our x range and is consistent with the CBT calculation.

4.2.3   Scaling models based on the EMC-SRC correlation

The observed correlation between the EMC effect and the contribution of SRCs [28, 11] has generated much interest and several ideas as to what underlying physics might connect these phenomena [11, 3, 31, 6, 23]. Unfortunately, we do not have associated calculations that provide detailed predictions for the EMC effect or its flavor dependence. We can, however, take various ideas that have been proposed to explain the correlation and use this to predict the scaling of the EMC in various nuclei [3].

Older parameterizations assumed that the EMC effect depended on the density, so density distributions for protons and neutrons in various nuclei can be used to make predictions of the relative size of the EMC effect in these nuclei, as well as predicting the flavor dependence based on the difference of the densities observed by protons and neutrons in the nucleus. More recent proposals include the idea that the local environment of the struck nucleon drives the EMC effect [21, 11, 6], and so the EMC effect would scale based on the local density for protons and neutrons in the nucleus, in which case the size of the EMC effect would be related to the probability for the struck nucleon to be close to another nucleon [3]. It has also be proposed that the EMC effect might be associated with high-virtuality nucleons [28, 11, 31, 6], in which case the size of the EMC effect could be estimated by examining quantities such as the fraction of the nucleon distribution at very high momenta, the average virtuality of the nucleons, or their average kinetic energy [3].

The flavor dependence associated with these scaling assumptions were evaluated in light nuclei, up to $A = 12$, using the one- and two-body momentum and density distributions from *ab initio* Quantum Monte Carlo Calculations [54]. The predicted A dependence of the EMC effect in light nuclei showed a clear difference between the assumption of scaling with average density and the other pictures [3]. By extracting proton and neutron distributions separately, we can also extract the difference in the proton vs. neutron
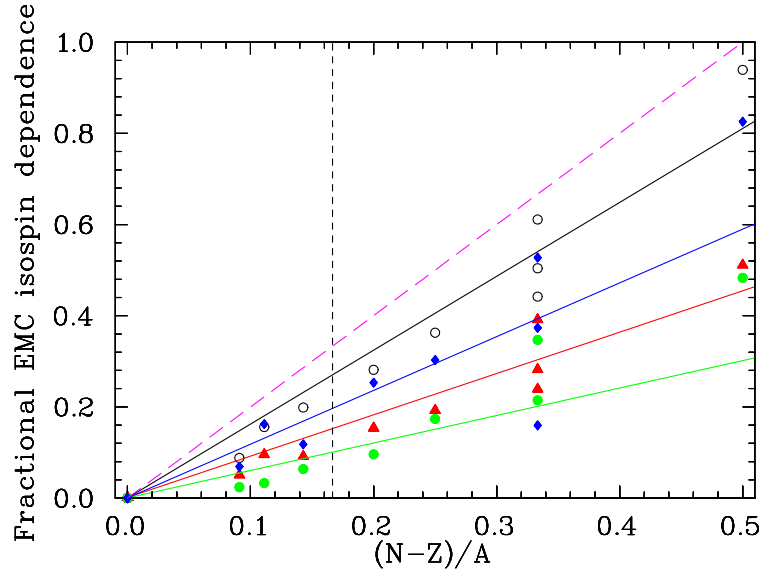
Figure 13: Isospin dependence of the EMC effect vs. fractional neutron excess of the nucleus for the four scaling models: fraction of momentum distribution above 300 MeV/c (black open circles), average kinetic energy (red triangles), average density (green circles), and probability to be within 1 fm of another nucleon (blue diamonds); the solid lines of the same color are simple unweighted linear fits. The dashed magenta curve is the 'upper limit' prediction taking 100% np-dominance in SRCs and assuming that the isospin dependence of SRCs translates directly to the isospin-dependence of the EMC effect. The vertical short-dashed line shows the (N-Z)/A value corresponding to ^{48}Ca [3].

EMC effect, shown in Fig. 13 as a function of the fractional neutron excess, along with linear fits to each of these scaling assumptions. The green points represent the prediction based on assuming that the EMC effect scales with average density seen by the protons and neutrons. While small, this model still yields a non-trivial flavor dependence. The other curves represent other scaling assumptions motivated by the observed EMC-SRC correlation, while the magenta dashed line corresponds to the upper limit one would expect based on the observed EMC-SRC correlation, taking 100% np dominance for SRCs and assuming that the relative size of the EMC effect in protons(neutrons) is identical to the fraction of protons(neutrons) in SRCs [28].

It is interesting to note that all of these simple scaling models yield the same qualitative effect, an enhanced EMC effect in minority nucleons, as does the CBT calculation. However, they differ significantly in the predicated size of the flavor dependence. The predictions based on the idea of scaling with density, local density or high virtuality predict an flavor dependence of 15-40% when evaluated at the neutron excess of ^{48}Ca. The CBT model, expressed in terms of this same flavor dependence, yields a 35% effect, while the idea that the EMC effect is driven directly by np-dominance of SRCs yield a 50% flavor dependence if total np dominance is assumed. The quantitative prediction is sensitive to the assumed underlying mechanism, with the size of the effect varying by a factor of three. As such, a direct measurement of the flavor dependence of the EMC effect is not only needed as input to a wide range of high-energy measurements on non-isoscalar nuclei, it also provides sensitivity to the underlying mechanism. In evaluating the sensitivity of the proposed measurement, we take the CBT model as the default model for a "large" flavor dependence,

but note that it will also be important to differentiate between a large effect and a smaller effect (roughly half the size) to have the ability to evaluate predictions within this range.

4.3 Sensitivity of the Proposed PVEMC Measurement

An evaluation of the statistical and systematic uncertainties for the PVEMC measurement is presented in Sec. 6. Figure 14 shows the projected uncertainties, along with predictions for a_1 assuming no flavor dependence along with a range of flavor-dependent models as discussed in the previous sections. The error bars shown include statistical and experimental systematic uncertainties, as well as uncertainties associated with model-dependent corrections relevant for the comparison of the data to the flavor-independent EMC effect hypothesis. We show the CBT model of the flavor dependence, the scaling models presented in Sec. 4.2.3, as well as some more 'extreme' assumptions for ease of comparison to projections from other experiments.
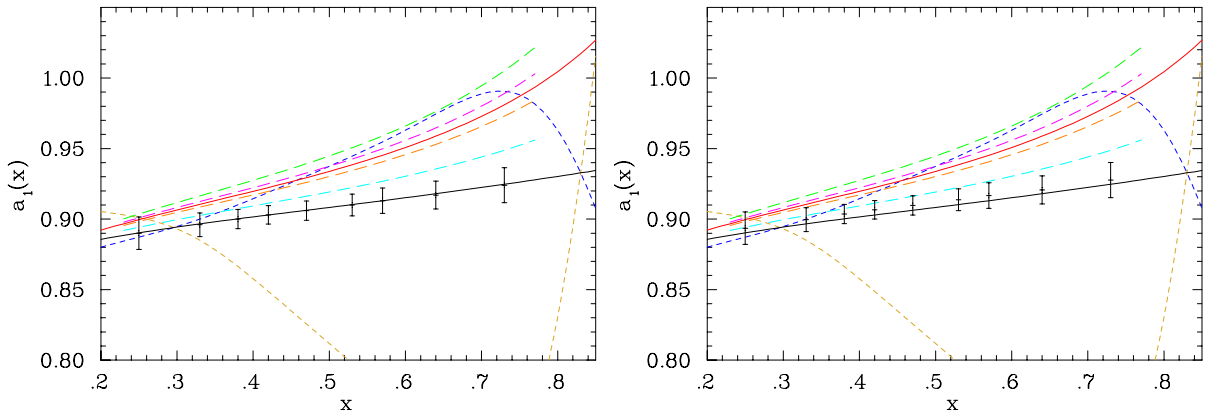

Figure 14: (Left) Projected a_1 data uncertainties (black points) generated assuming a flavor-independent EMC effect (solid black curve). The red line is the CBT model, the long-dashed curves correspond to the scaling predictions of Sec. 4.2.3, and the short-dashed lines assume the EMC effect occurs entirely within the up or down quarks. (Right) Same, with the data shifted towards the CBT calculation by the 0.4% to illustrate the impact of the normalization uncertainty

To determine the sensitivity of the measurement, we compare the null (flavor-independent) hypothesis to projected data generated according to the CBT model. Neglecting the normalization uncertainty, this yields $\chi^2 = 62.6$ for 9 degrees of freedom, a 7.9σ deviation from the flavor-independent prediction. Shifting the data down by the normalization uncertainty yields a 7.1σ deviation, while a shift of twice the normalization uncertainty still correspond to a 6.6σ signal. We treat this as a conservative estimate of the ultimate sensitivity, as it is the sensitivity obtained assuming an arbitrary 2σ shift of the normalization.

The CBT model yields a relatively large flavor dependence compared to other estimates provided in Sec. 4.2.3, with an EMC flavor asymmetry of 0.35, with other estimates ranging from 0.15-0.50. Thus, the 6.6σ sensitivity to the CBT calculation also corresponds to a 3σ sensitivity for even the smallest of these estimates, and a $>6\sigma$ difference between the largest and smallest predictions in this range. **Thus, it has both excellent discovery potential for flavor dependence and the precision to differentiate between models that predict larger or smaller flavor dependence.** This level of precision will provide significant constraints on the impact of the flavor dependence on other observables involving high-energy processes on non-isoscalar nuclei, and reduce the uncertainties associated with possible flavor dependence for the processes discuss in Sec. 3.4.

4.4 Relation to Other Experiments

4.4.1 JLab E12-10-008

Measurements of the EMC effect for ^{40}Ca and ^{48}Ca and other targets will be taken in JLab experiment E12-10-008 [13], and the ratio of ^{48}Ca to ^{40}Ca has some sensitivity to the flavor-dependence of the EMC effect. We quantify the significance of the measurement by taking projected data following the CBT model and examining the χ^2 between the data and the flavor-independent prediction in the EMC effect region, $0.3 \leq x \leq 0.7$. For the projected data, we take 0.7% point-to-point systematic uncertainties, 0.95% statistical uncertainties, and a 1.4% normalization uncertainty on the ratio, based on the proposal [13]. The projected data yield a 2.1σ deviation from the flavor-independent model if we neglect the normalization uncertainty. Allowing for shifts in the normalization, we find that shifting the data by 80% of the normalization uncertainty yields χ^2 values that are are equally good for the flavor-independent and CBT models, meaning that direct chi-squared comparison is not useful when taking the normalization uncertainty into account. To minimize the impact of a large normalization uncertainty, we examine the slope of the data between $x = 0.3$ and 0.7. The projected error bars yield an uncertainty in the slope of ± 0.025, compared difference between the CBT and flavor-independent predictions of 0.047, yielding only a 1.9σ sensitivity to the CBT flavor dependence.

The numbers above are made based on the proposed EMC effect measurements. We repeated the exercise assuming a factor of four increase in statistics to evaluate the sensitivity of an improved measurement that is limited by the assumed systematic uncertainties rather than the statistics. With the improved statistics, the point-to-point uncertainties are reduced by a factor of 1.37. This corresponds to a 2.6σ sensitivity based on examining only the slope, compared to the 1.9σ sensitivity for the measurement as proposed. With the improved statistics, neglecting the model dependence of the isoscalar correction and A dependence of the EMC effect will have a larger impact on the final result than for the measurement as proposed. Taking an uncertainty of 0.01 on the values of F_{2n}/F_{2p} used for the isoscalar correction (to be consistent with what was assumed for the PVEMC model dependence) yields a small model-dependent uncertainty in the comparison of ^{48}Ca to ^{40}Ca, decreasing the sensitivity by 10% and yielding a final sensitivity to the CBT prediction of 2.3σ.

Figure 15 shows projected results for the ^{48}Ca/^{40}Ca cross section ratio (with the assumed increase in statistics) in the region of the EMC effect, where the ^{48}Ca result has had isoscalar corrections applied. The solid black line is the predicted impact of the A-dependence from the SLAC global fit [27], the red line shows the prediction of the CBT model, and the long-dashed lines show the predictions for the scaling models and upper limit described in Sec. 4.2.3.

A direct comparison between the two is given in Table 1. The small signal of flavor dependence in the ^{48}Ca/^{40}Ca ratio, combined with the 1.4% normalization uncertainty, significantly limit the sensitivity of such comparisons. The proposed measurements will yield only $\sim 2\sigma$ differentiation between the CBT model and no flavor dependence, with $<3\sigma$ sensitivity even with significantly improved statistics, and do not have the ability to provide any meaningful differentiation between larger or smaller flavor dependence signals. If we see no signal of flavor dependence, we do not have 3σ sensitivity to anything except the 'upper limit' estimate of Sec. 4.2.3. If the ratio is consistent with the CBT result, it's only 2.3σ from the flavor-independent prediction, and 1-1.5σ from all other models, as shown in Fig. 4 (Sec. 2). **As such, the PVEMC data will be critically important no matter what is observed in the ^{48}Ca/^{40}Ca ratios.**

While E12-10-008 will measure other nuclei, the calcium comparison is the most sensitive test. For heavy nuclei such as Au and Pb, the size of the EMC effect is somewhat larger, as is the fraction neutron excess, but there is no isoscalar 'baseline' available for comparison. Lighter nuclei show a smaller EMC effect and generally have smaller neutron excesses, yielding smaller sensitivity to flavor dependence. They have
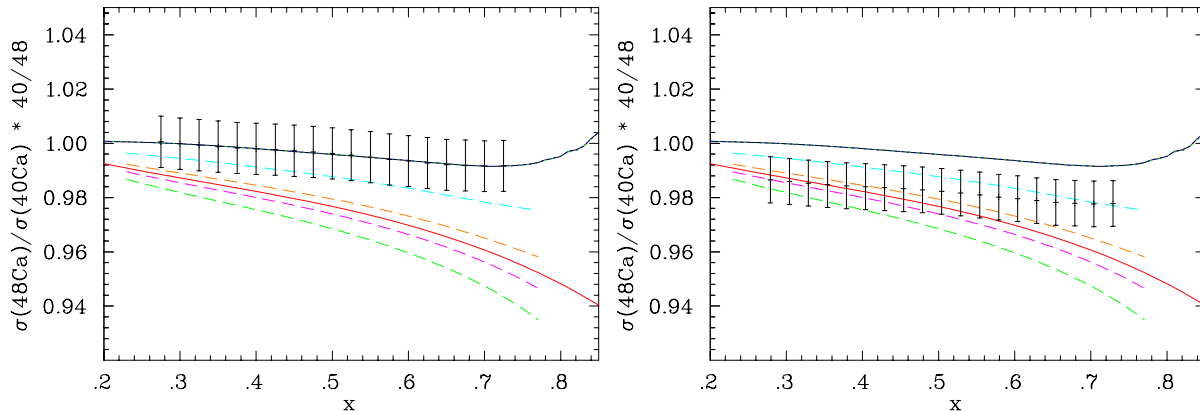
Figure 15: (Left) Projected calcium cross section ratio uncertainties (black points) based on a flavor-independent EMC effect (solid black curve) *and assuming a factor of four increase over the proposed statistics of the E12-10-008 measurement.* The red line is the CBT model, the long-dashed curves correspond to the scaling predictions of Sec. 4.2.3, and the short-dashed lines assume the EMC effect occurs entirely within the up or down quarks and are identical to the flavor-independent result because they are constructed such that the total EMC effect is unchanged. (Right) Same, with the data shifted towards the CBT calculation by the 1.4% to illustrate the impact of the normalization uncertainty.

the the additional complication that the A dependence in light nuclei is less well understood, as contributions related to clustering and/or short-range correlations are strongly A dependent in light nuclei.

4.4.2   JLab PR12-09-004, C12-21-004 - SIDIS

Proposal PR12-09-004 [43], "Precise Measurement of π^+/π^- Ratios in Semi-inclusive Deep Inelastic Scattering Part II: Unraveling the Flavor Dependence of the EMC Effect", aimed to use a comparison of π^+ and π^- production from Au to look for flavor dependence in the EMC effect. The proposal was deferred, in large part due to questions about how well the data could be interpreted in terms of flavor dependence, given the possibility for differences in hadron attenuation effects for π^+ and π^- as well as questions regarding possible differences in the p_T dependence of the pion yields since the proposed measurement would only detect pions emitted along the virtual photon 3-momentum. The degree to which factorization in the SIDIS reaction would be satisfied was also a concern.

C12-21-004 [14], "Semi-Inclusive Deep Inelastic Scattering Measurements of A = 3 Nuclei with CLAS12 in Hall B", raised the idea of comparing π^+ and π^- production from ^{3}H and ^{3}He. While the EMC effect is significantly smaller in these nuclei, the comparison of mirror nuclei minimizes the uncertainties associated with nuclear effects. While the CBT calculation uses a mean-field approach and cannot provide reliable predictions for A=3 nuclei, estimates based on an extreme model of flavor dependence (EMC effect generated entirely by down quark modification) showed an observable signal of flavor dependence as shown in the left panel of Figure 16. However, this extreme assumption is inconsistent with all of the models we discuss in Sec. 4.2, for which the proton (or up-quark) EMC effect would be enhanced in ^{3}H and suppressed in ^{3}He. An updated estimate, assuming a realistic EMC effect where the proton EMC effect is twice that of the neutron for ^{3}H (and half for ^{3}He), yields a near-total cancellation between the effects in ^{3}H and ^{3}He, as shown in the right panel of Fig. 16.

Projections from [14] are shown in Fig. 17 in which ratios to deuterium for the charged pion sum ($\pi^+ + \pi^-$) and difference ($\pi^+ - \pi^-$) for ^{3}He and ^{3}H are shown. The error bars on the projected data points include
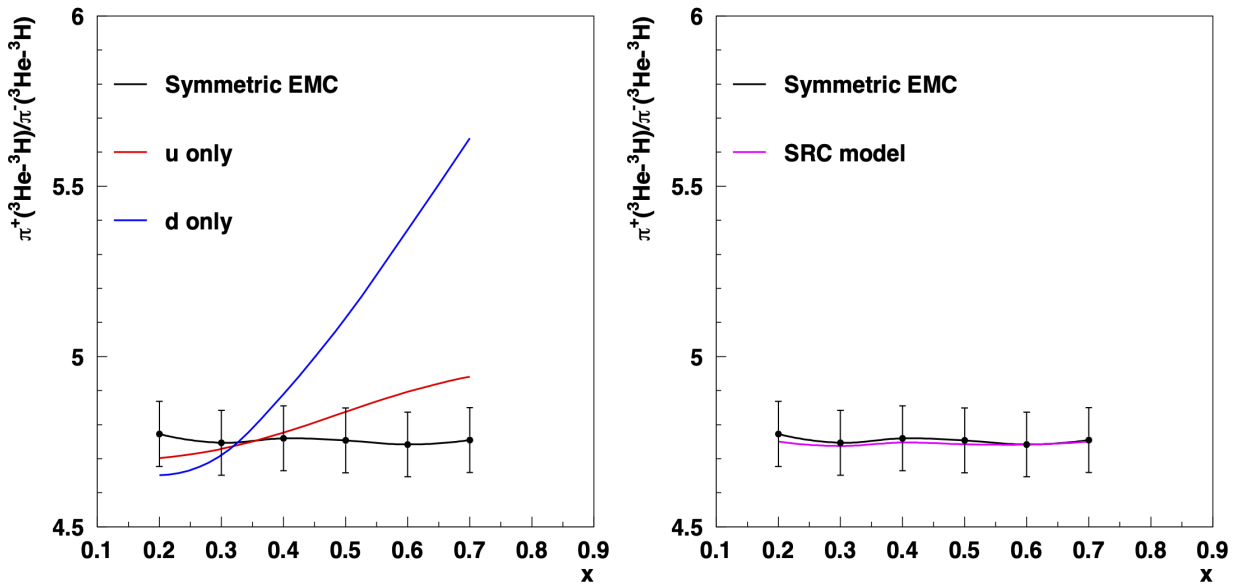
Figure 16: Projected impact of flavor dependence of the EMC effect on the comparison of π^+ and π^- production from ^{3}H and ^{3}He. The left panel shows the prediction from a flavor-independent EMC effect (black curve) compared to the prediction assuming that the EMC effect is carried entirely by the up (red) or down (blue) quarks. The right panel shows the same observable assuming the flavor dependence based on Ref. [5] (magenta), indicating no sensitivity in this more realistic flavor dependence.

only statistical uncertainties. The largest effects are typically at the 3-5% level, with the down-only and KP curves being the only predictions that show effects of this size. As noted above, the down-quark only EMC effect is both an extreme assumption and inconsistent with models of the EMC effect. The KP curves shown here are slightly different from the nuclear effects of the Kulagin-Petti model [47]. In the proposal, they take the KP evaluation of the nuclear effects in ^{3}H and ^{3}He, but treat this as a *flavor-independent* modification of the pdfs in each of the two nuclei [14].

We leave it to the C12-21-004 collaboration to provide a final evaluation of their sensitivity, including model-dependent corrections relevant for the comparison to models of the flavor dependence, as requested by the PAC. However, we note that a detailed evaluation of the systematic uncertainties and target normalization will be important in determining the ultimate sensitivity. First, because of the small size of the effects, typically 3-5%, based on the predictions in the proposal [14], but also because the observables often include differences, (π^+ - π^-) or (^{3}H - ^{3}He), which can yield significant amplifications of the statistical and systematic uncertainties. In addition, as with the inclusive ^{48}Ca/^{40}Ca ratios, allowing for a normalization shift in the target ratios will further reduce the sensitivity to flavor-dependent effects.

4.4.3 AMBER - Drell-Yan

The AMBER (formerly COMPASS-II) [55, 56] experiment has proposed measuring π-induced Drell-Yan with carbon and tungsten targets. These data will provide a complementary measurement covering x values lower than all but the lowest x point of the proposed measurements. Specifically, their initial phase is designed to separate valence- and sea-quark contributions to *pion* structure by measuring both the π^+ and π^-
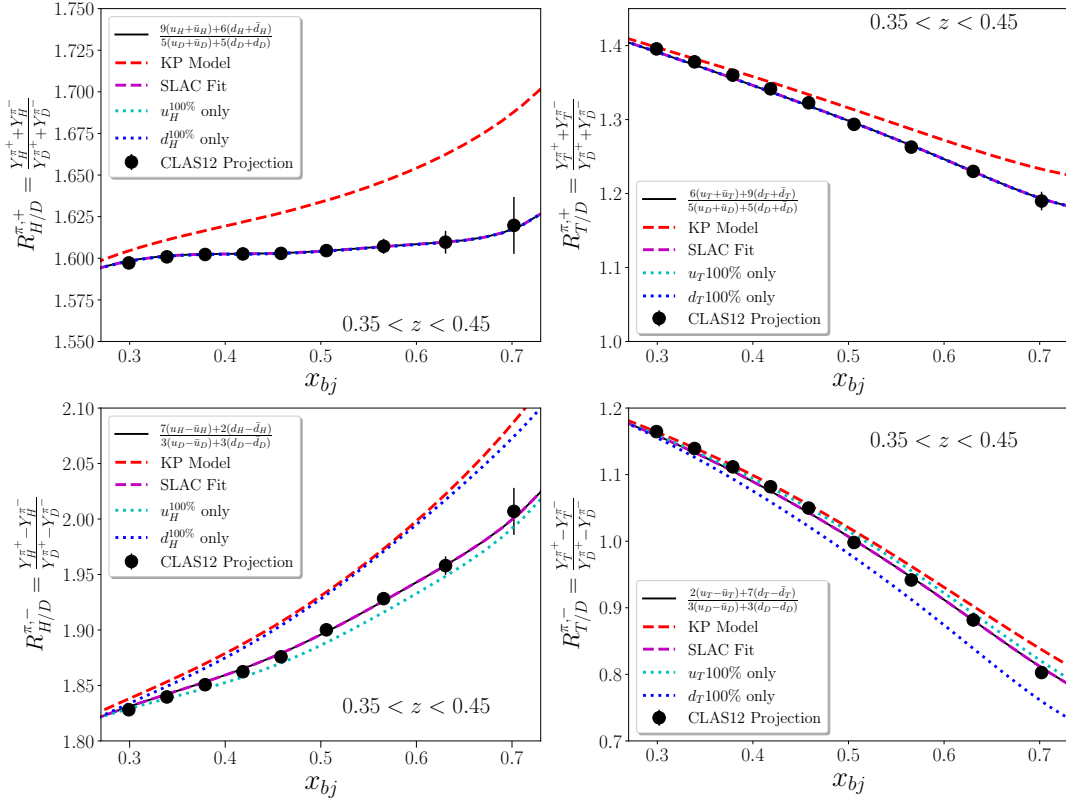
Figure 17: Projected charge-sum (top plots) and charge-difference (bottom plots) ratios to deuterium for ^{3}He (left) and ^{3}H (right) for several calculations from [14]. Only statistical uncertainties are included.

absolute cross sections on carbon and tungsten targets. AMBER data will cover the range $0.08 \leq x_2 \leq 0.34$, meaning that there will be minimal overlap between their data and the proposed PVEMC measurement.

The AMBER kinematic coverage makes it very complimentary to the proposed PVEMC measurement, as AMBER will cover the low-x region. This is the region where many of the models examined here predict smaller flavor dependence, but the use of a heavy target may provide a larger signal. Forming the ratio of $\sigma^{\pi^+ A}/\sigma^{\pi^- A} \approx d^A/(4u^A)$ gives some sensitivity to the flavor dependence of the nuclear EMC effect. Here, "approximately" represents simplifications from leading order, and from ignoring the sea quarks in the proton. With their tungsten target, AMBER's statistical uncertainty on the ratio will be approximately $\pm 5\%$, which can be compared with the uncertainties from previous measurements shown in Fig 10. In addition to the statistical uncertainty, there will be systematic uncertainties and model-dependent corrections that need to be applied.

AMBER has also proposed to measure the ratio of the difference between π^+ and π^- cross sections on carbon and tungsten targets, i.e. $\frac{\sigma^{\pi^+ C} - \sigma^{\pi^- C}}{\sigma^{\pi^+ W} - \sigma^{\pi^- W}}$, which gives the ratio of the valence distributions, measured to between $\pm 2\%$ and $\pm 5\%$. Additionally, in this super ratio, the systematic uncertainty from nuclear effects in the PDFs is estimated to be 4%. The ratio $\sigma^{\pi^- W}/\sigma^{\pi^- W} \approx u^C/u^W$ can also be formed with the proposed AMBER data [19] and will also be measured to 2–5%[57].

5   Experimental Design

We choose a $2.4 \, \mathrm{g/cm^2}$ ^{48}Ca target ($x/X_0 = 12\%$) at $80 \, \mu$A with maximum longitudinal beam polarization as the general production conditions. **The experimental layout we propose is identical to the existing SoLID PVDIS proposal [50], with the replacement of the LD$_2$ target ladder with our ^{48}Ca target ladder.** For 68 days of production, a 0.7-1.3% statistical uncertainty for $0.2 < x < 0.7$ can be obtained (Fig. 18). A 0.6-0.7% systematic uncertainty per-bin is anticipated, discussed in Sec. 6.2. Our sensitivity to the CBT model is shown in Fig. 14 and is $\sim 8\sigma$ neglecting normalization uncertainty, and 7σ if we arbitrarily apply a one-sigma shift in the normalization to minimize the signal.
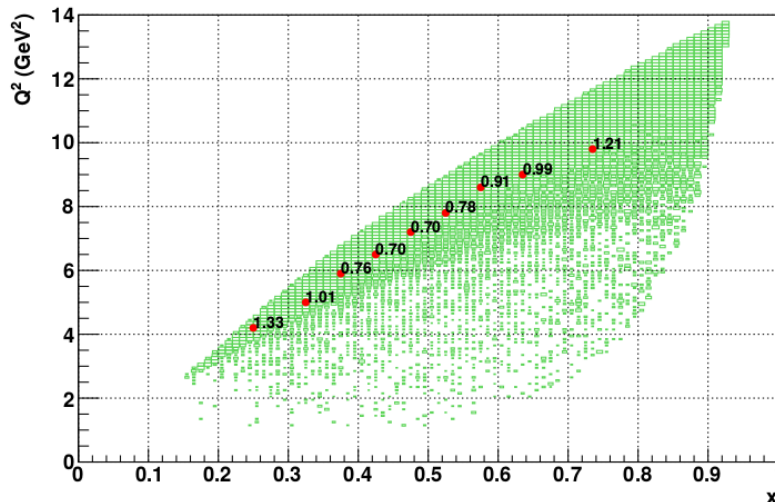

Figure 18: Our statistical precision for A_{PV} for x and Q^2 bins in %.

This is a true "counting mode" parity-violating experiment in contrast to parity-violating experiments in the past that have used integrating detectors gated over the beam-helicity window. The full SoLID program is still under a detailed design and review process, which is more fully described in the SoLID pre-CDR document [58]. Here we cover the relevant aspects of the design and the anticipated performance.

Most aspects of this experiment are less demanding than the approved PVDIS LD$_2$ experiment for the following reasons:

- this proposal utilizes a solid target with good thermal properties and is not subject to effects such as boiling,

- less total target material mass, generally providing lower rates,

- the physically short target has better controlled acceptance and collimation.

This target has a 12% radiation length, which is a factor of two larger than the LD$_2$ target, and presents a few challenges. First, the overall radiative corrections due to external bremsstrahlung is approximately doubled. Direct photons from the target are increased as well as the pion photoproduction rates. Combined with the fact the target has a neutron excess, the relative number of π^- to DIS events is increased. A suite of simulations has been developed in the Geant4 framework which includes a complete and detailed representation of the target and detector geometries, Fig. 19, and includes particle showering and optical photon production. In addition, event generators for deep inelastic scattering based on the CTEQ6M
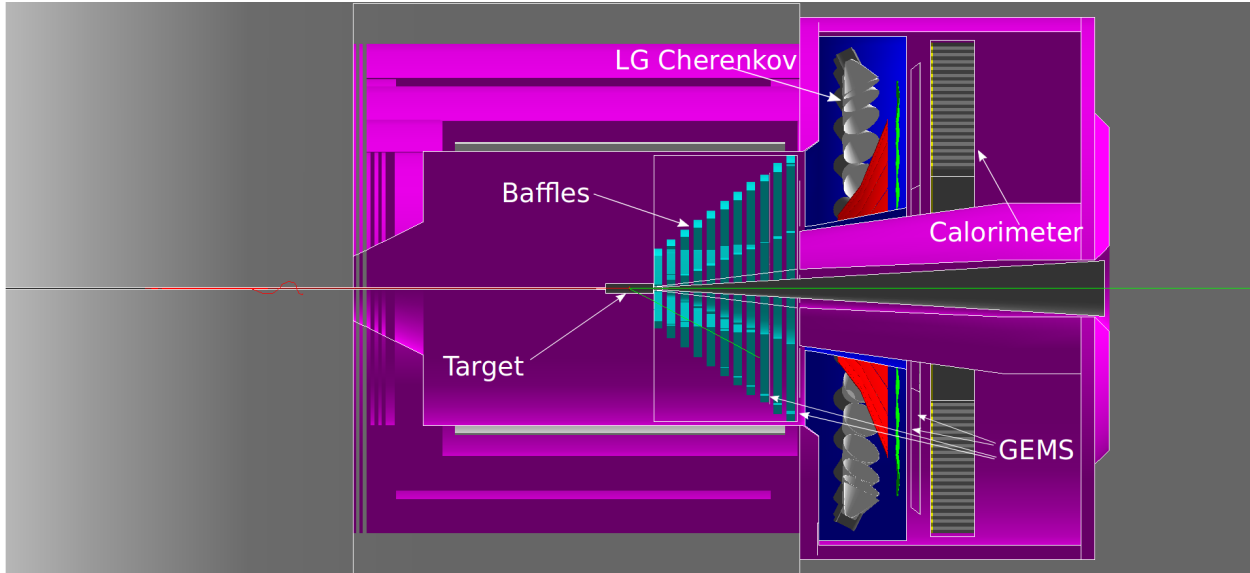
Figure 19: SoLID side-view of the Geant4 configuration with full detector setup.

PDFs [59] and pion production based on a SLAC photoproduction data parameterization [60] with the equivalent photon approximation for the electroproduction data have been developed. We utilize this simulation to generate the following rate and response estimates.

5.1 Targets

We propose to use a 2.4 g/cm^2 ^{48}Ca target, assumed to be 93% isotopically pure. A 0.8 g/cm^2, 90% pure target was employed by the $x > 2$ experiment [61] at 50 μA, Fig. 20. The CREX experiment [62] ran with beam current of 150 μA at 2.2 GeV on a 2.4 g/cm^2 95.99% pure ^{48}Ca target with 3.84% ^{40}Ca impurities. The target design used in previous experiments will need to be modified to allow for full acceptance of all scattering angles when the raster is employed.

Calcium has relatively robust thermal properties which are advantageous for this experiment: a melting point of 840° C and a high thermal conductivity of 200 W/m/K. While the melting point is an absolute upper limit, calcium undergoes crystalline structure changes at lower temperatures. A 4×4 mm^2 raster will be used to distribute the heat load. This experimental configuration will have a power deposited from the beam of about 600 W, but thermal calculations showed that with sufficient cooling on the support frame held at room temperature, operate at only 100° C, within heating limits and below the CREX ΔT.

The original design was a disk with a diameter of at least one inch so that detected electrons would not pass through the target holder (left panel, Fig. 21). Since the previous submission, we have modified the target design to significantly reduce the amount of ^{48}Ca needed, while maintaining the same thickness and reducing multiple scattering. Rather than a disk with a uniform radius, the radius will reduce along the length of the target, significantly reducing the amount of target material. The holder of the target, made of beryllium or aluminum, will have to be thick enough to allow sufficient heat conduction out of the target, but the added thickness will be significantly less than the amount of calcium removed, reducing both multiple scattering and radiation for the outgoing electron. We estimate that this design will allow us to reduce the amount of ^{48}Ca used by 30% or more, with no negative impact on the physics measurement. A detailed analysis of the heat transfer through the target holder will be required to finalize the design, but the target group does not believe that there will be issues obtaining sufficient mechanical support or heat conduction [63].
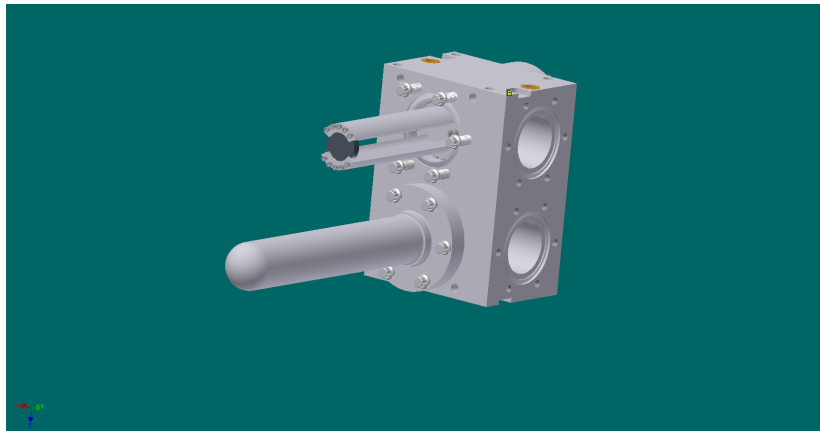
Figure 20: A CAD design of the existing ^{48}Ca target for E08-014. Two identical ^{40}Ca and ^{48}Ca targets were mounted in the ladder design.

We do not anticipate the lab having to buy new material for the target. The target group plans to recover ^{48}Ca from the existing supply at JLab, and it is estimated that the existing material would be sufficient to provide the target as proposed. The calcium recovery would take some time and developing the needed systems could presumably begin shortly after the experiment is approved. Additional ^{48}Ca would need to be acquired only if sufficient material is not recovered from the existing targets, and presumably only a small fraction of the total ^{48}Ca required would have to be purchased.

Auxiliary targets will be required in the same ladder to provide calibrations and tests, described in Sec 5.4. In particular, a set of several carbon foils spaced ± 20 cm (with one specifically at the center position of the ^{48}Ca target). Aluminum targets with known radiation thicknesses of 1%, 5%, and 10% will help provide validation of unfolding external radiative effects and a LH$_2$ target will be used for momentum calibration.

5.2 SoLID

The SoLID project is a large acceptance, high luminosity spectrometer and detector system designed for experiments that require a broad kinematic acceptance at high rates. It presently has five approved experiments covering physics topics such as PVDIS on LD$_2$ and LH$_2$, semi-inclusive DIS on polarized targets, and J/ψ production at threshold. We will focus on the PVDIS configuration, which consists of

- A 3 m diameter solenoidal magnet that provides a central field of ~ 1.5T and field integral of about 1.8 T $\cdot$ m.

- A set of collimators ("baffles") which block low momentum particles and line-of-sight photons.

- A set of five GEM layers which provide high resolution, hit-based tracking in a high luminosity environment.

- A light gas Cherenkov detector for pion identification.

- An electromagnetic calorimeter in a shower-preshower configuration which also provides some pion rejection capabilities and acts as the primary trigger and an additional point in tracking.

This configuration with baffles nominally has 2 rad azimuthal acceptance, polar angle acceptance of 22-35°, and momentum acceptance of $1-7$ GeV. Azimuthally it is divided into 30 predominantly independent
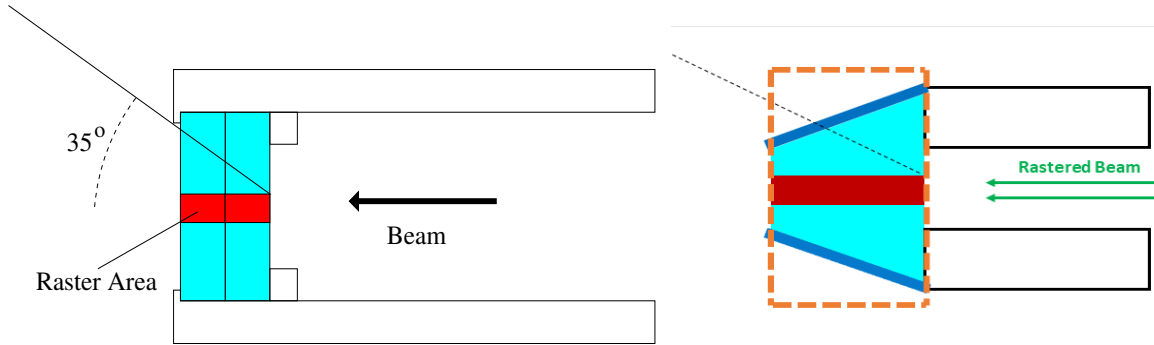
Figure 21: Schematic drawings of the old (left) and new (right) target design concepts. In the old design, the target was a disk of a least 1 inch diameter. In the new design, the calcium is pressed into a conic section made of beryllium (or aluminum). The orange box in the new design indicates the size of the ^{48}Ca disk in the original design. While the outgoing electrons now go through the target holder (estimated to be 1.5-3mm to allow for sufficient heat conduction), this will yield less multiple scattering and radiation length due to the reduced amount of calcium.

sectors which can operate at a total of $\sim$ 600 kHz in inclusive running. A representation of this setup from our Geant4 simulation is shown in Fig. 19.

5.2.1 Baffles

The baffles provide a reduction in the large low-momentum flux and block line-of-sight photons from the downstream detectors. They consist of 11 lead "wheels" which divide the acceptance into 30 sectors, Fig. 22. The curvature of the arms are designed in such a way that particles within a specific momentum window will pass in between the arms to the detectors.

The coverage of the baffles defines the azimuthal and momentum acceptance for the spectrometer. Nominally, the first baffle reduces the flux by a factor of two and particles less than 1 GeV are blocked by successive baffles, leading to an overall charged rate reduction of about an order of magnitude. The momentum acceptance for the accepted particles follows from several geometric and design effects and is shown for the ^{48}Ca configuration in Fig. 23.

5.2.2 GEMs

The GEM (gas electron multiplier) trackers originally developed at CERN provide high resolution tracking in high rate environments. They have been demonstrated to work at rates up to 100 MHz/cm^2 and provide a hit resolution up to 70 μm with a 200 μm readout pitch. We employ five planes of GEM chambers, three interleaved with the rear baffle planes and two after the light-gas Cherenkov detector, detailed in Table 2. Each plane consists of 30 individual GEM modules and are aligned such that the gaps of the first three chambers lie over a baffle spoke, Fig. 24. The pitch will be 0.4 mm for the first three GEMs and 0.6 mm in the rear GEMs as the rates are lower.

Significant contributions to the GEM rates come from not only DIS electrons, but also π^- and photons. For the latter, the response is highly dependent on the photon momentum and the radiation thickness of the detector. Figure 25 shows the results from Geant4 simulation for the photon response with a 0.5% radiation length GEM, which drops for photons < 1 MeV. A comparison between hit rates for our proposal and simulations for the LD$_2$ measurement are shown in Table 3.
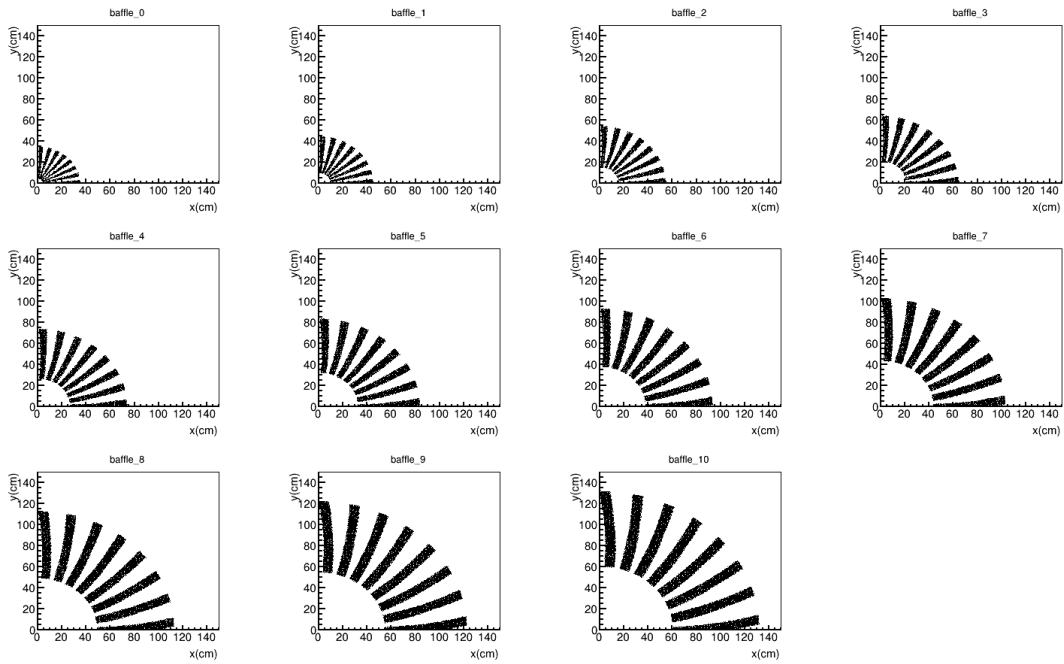
Figure 22: Projection of the baffle lead "spokes" to block low momentum particles.
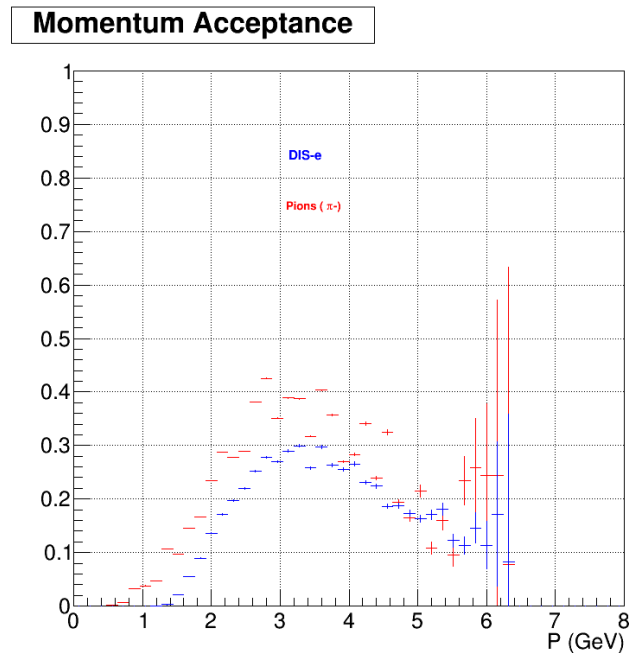
Figure 23: Electron and π^- acceptances from the baffles. Differences between these are due to varying angular distributions and the fact that π^- have longer interaction lengths.
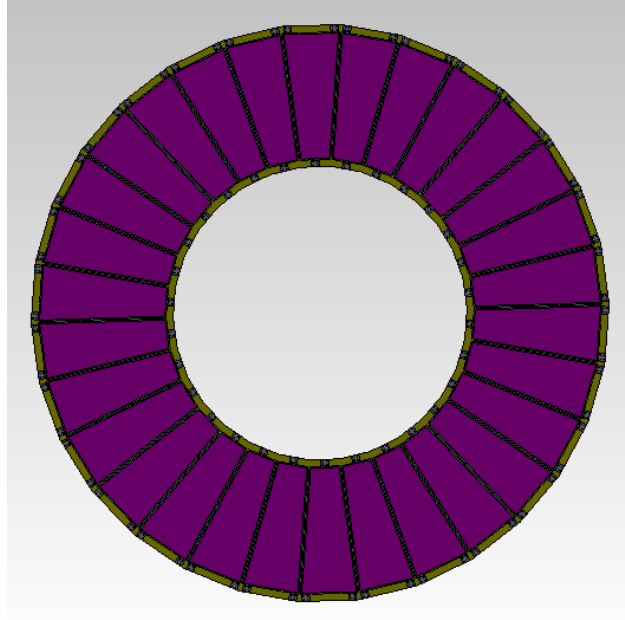
Figure 24: CAD drawing of a GEM plane for the PVDIS configuration.

Location	Z (cm)	R_{min} (cm)	R_{max} (cm)	Surface (m^2)	# chan
1	157.5	51	118	3.6	24 k
2	185.5	62	136	4.6	30 k
3	190	65	140	4.8	36 k
4	306	111	221	11.5	35 k
5	315	115	228	12.2	38 k
Total				≈ 36.6	≈ 164 k

Table 2: GEM design parameters for the SoLID PVDIS configuration.
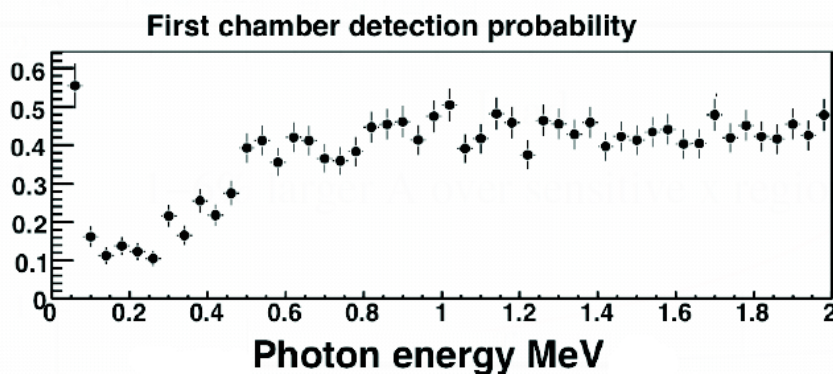
Figure 25: Geant4 calculation results for photon interaction probabilities with GEM chambers from Ref. [64].

GEM plane	LD$_2$ background (kHz/mm^2/μA)	^{48}Ca EM background (kHz/mm^2/μA)	^{48}Ca EM background (no baffles) (kHz/mm^2/μA)
1	6.8	4.8	49.4
2	3.0	2.1	32.3
3	1.1	0.8	9.9
4	0.7	0.5	6.4

Table 3: The low energy EM background radiation at GEM detectors compared for ^{48}Ca and LD$_2$ targets with and without baffles.

| Momentum range (GeV)	π^- (MHz)	π^+ (MHz)	$\pi^0(\gamma)$ (MHz)	Proton (MHz)	EM (γ, e$\pm$) (GHz)
p > 0.0 GeV	618	283	70123	483	844
p > 0.3 GeV	439	153	438	417	n/a
p > 1.0 GeV	123	18	37	51	0.0
p > 3.0 GeV	2	0.01	0.04	0.004	0.0

Table 4: Breakdown of rates based on the particle types for ^{48}Ca target at 80 μA.

The radial GEM rates are presented in Fig. 26. The particle rates at the last GEM, which will be incident on the EM calorimeter, are broken down by particle type and shown in the Table 4. The initial π^+ background is heavily suppressed by the combination of baffle design and the solenoidal magnetic field but will also be produced in interactions within the baffle material. A combination of triggering and off-line analysis is required to suppress the π^- background to desired level. The DIS electron rates at the last GEM for various x-cuts is shown in the Table 5.

The background rates are much greater than the DIS rates at the entrance to the EM calorimeter. The rates below p < 1.0 GeV are predominantly electromagnetic backgrounds. The high energy p > 1.0 GeV backgrounds are dominated by contributions from pions and protons.

5.2.3 Calorimeter

The electromagnetic calorimeter serves as the primary trigger as well as an independent means for rejecting π^- backgrounds. It it configured in a hexagonal preshower-shower configuration and consists of "shashlyk"-style blocks with 50 cm of interleaved sampling lead and scintillator plates with a fiber readout, Fig. 27, with a radial coverage of 110-265 cm or $\sim$18 m^2. Each module has a lateral coverage of about 100 cm^2

Momentum range (GeV)	^{48}Ca (kHz)
DIS Total	228
W > 2.0 GeV, x$_{Bjk}$ > 0.20	207
W > 2.0 GeV, x_{Bjk} > 0.55	15
W > 2.0 GeV, x_{Bjk} > 0.65	3

Table 5: Breakdown of DIS rates for ^{48}Ca target at 80 μA.
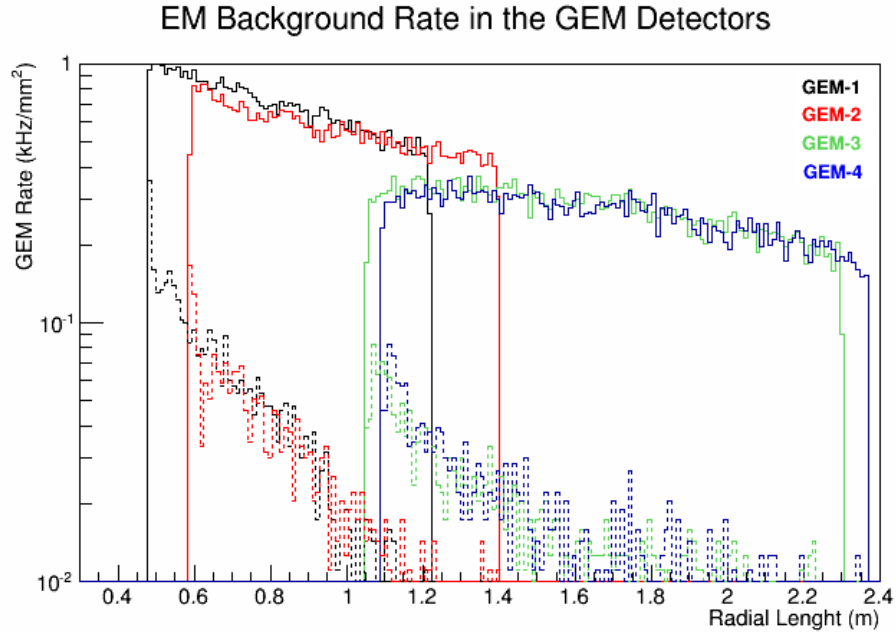
EM Background Rate in the GEM Detectors

Figure 26: The design of the baffle structure minimizes the EM background rates at the GEM detectors. The solid lines shows background rates with no baffles and the dashed lines show the rates with the baffles. The baffle structure reduce the background rates by almost a factor of 10.

providing adequate position resolution, background sensitivity, and cost for a total of about 1800 modules. The shower and preshower are read out through 100 1-mm-diameter waveshifting fibers that are threaded down the module and run to the rear of the solenoid. They are coupled to clear fibers and then to multianode PMTs (1 PMT per module).
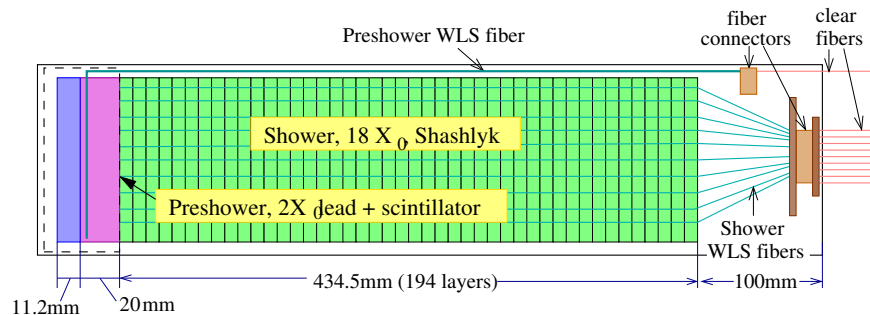
Figure 27: Cross section of an electromagnetic calorimeter module and absorber sheets.

The momentum resolution requirements for the shower are relatively modest, as it must primarily provide a trigger above the low energy background flux, and reconstruct a reasonably good position and energy. For our modules, a $4\%/\sqrt{E}$ resolution has been simulated. A good position resolution is important as in the high luminosity environment, the reconstructed point will serve as a base for track reconstruction. Accounting for the energy distributions of tracks that are not normal to the face of the detector leads to a RMS of <1 cm is achieved in the radial and azimuthal directions.

Figure 28: π^- rejection and electron efficiency for calorimeter. Red points and curves are for calorimeter in PVDIS configurations

As a method of pion rejection (in combination with the gas Cherenkov), the preshower and shower energy deposition information can be used. For our configuration, at a 100:1 rejection factor is anticipated (improving with particle momentum) for $E > 2$ GeV, Fig. 28 while maintaining a 95% electron efficiency.

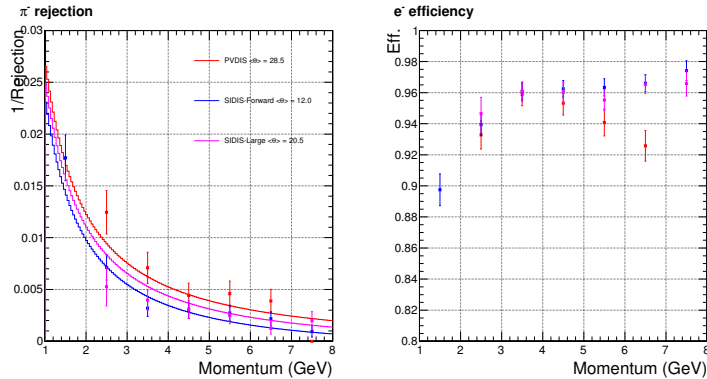Our simulations to determine the performance of the EM calorimeter are based on DIS events with realistic backgrounds incident on the EM calorimeter. These simulations provide trigger efficiencies for DIS electrons and all the background types. The trigger efficiencies and rates on particles incident on the full coverage of the EM calorimeter are used to extract the total trigger rate for the EM calorimeter. In order to further optimize the calorimeter performance, each $12°$ azimuthal sector in the calorimeter is divided into two $6°$ segments based on the background rate which varies due to the baffle structure. The low (high) rate section is shown in the top (bottom) panels of Fig. 29.

It is observed by dedicated EM calorimeter simulations that the pile-up effects are not significant for particles with momentum $p > 1$ GeV but is an important effect for particles with $p < 1$ GeV. Due to this effect, the trigger rates for the lowest energy particles cannot be broken down to particle type in a straight forward manner and we quote only a total trigger rate. Table 6 summarizes this for ^{48}Ca target.

See section 7.2.1 for the estimation of radiation dose in the Calorimeter

5.2.4 Light Gas Cherenkov

The light gas Cherenkov detector provides rejection of π^- background, which is difficult to otherwise suppress from the e^- DIS signal. In the PVDIS configuration, it is proposed to consist of a ~ 1 m gas radiator of 65% C_4F_8O and 35% N_2 (refractive index 1.001 or $\pi^\pm$ threshold of 3.2 GeV) and is divided up into 30 sectors matched to the baffle segregation. For each sector there are two spherical mirror sections to provide light collection over a broad radial range which focus into a Winston cone/PMT set (see Figure 30). The PMTs are 8×8 pixel multi-anode bialkali PMTs arranged in a 3×3 array and are shielded from the residual field with a mu-metal cone. To help reject pion triggers, the Cherenkov is placed in coincidence with the calorimeter through a sum of all 9 PMTs.

The photoelectron distributions generated as a function of angle for DIS electrons is shown in Fig. 31. A threshold was chosen dependent on the momentum where the pion rejection efficiency was maximized while losing minimum number of electrons and is shown in Fig. 32. The rejection factor for 2-3 GeV pions is 1000:1 - 400:1, worse for the higher energy π. In combination with the 100:1 independent rejection factor from the preshower/shower providing an overall rejection of 10^5 - 4×10^4 up to 3 GeV and at least 100:1
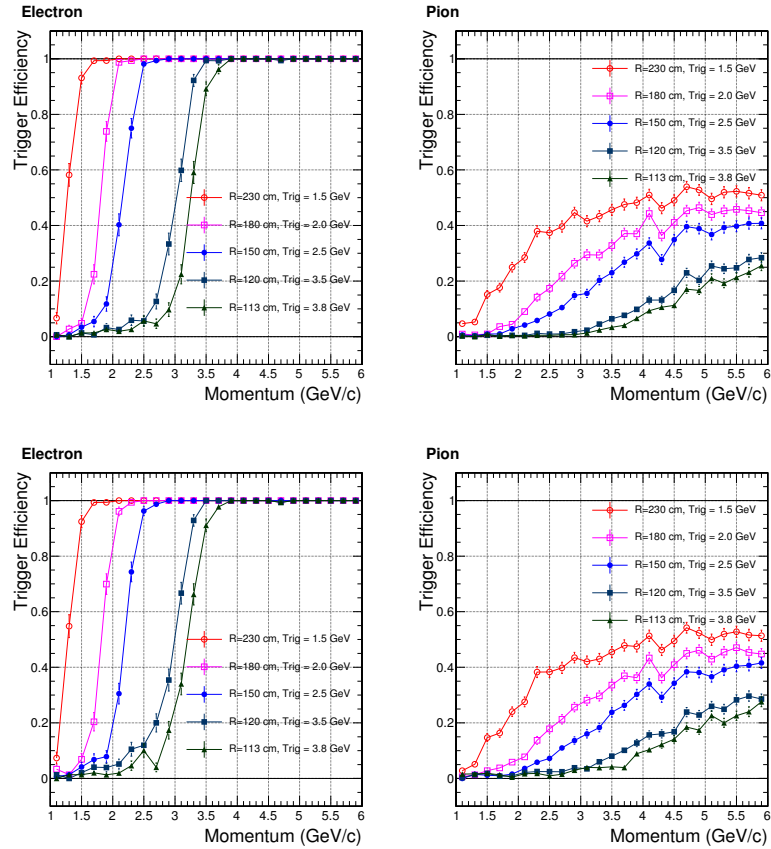
Figure 29: Electromagnetic calorimeter trigger performance for the low rate azimuthal region for e^- (left) and π^- (right). Top figures are for the low rate section; bottom for the high rate.

above that. The total rates seen by the Cherenkov and the estimated trigger rates are summarized in the Table 7. The π^-/e^- ratio we anticipate as a function of momentum is shown in Fig. 33 for both the LD$_2$ measurement and ^{48}Ca.

region	full	high	low
Rate entering the EC (kHz)			
e^-	240	129	111
π^-	5.9×10^5	3.0×10^5	3.0×10^5
π^+	2.7×10^5	1.5×10^5	1.2×10^5
$\gamma(\pi^0)$	7.0×10^7	3.5×10^7	3.5×10^7
p^+	4.8×10^5	2.1×10^5	2.7×10^5
sum	7.1×10^7	3.6×10^7	3.6×10^7
Rate for $p < 1$ GeV (kHz)			
sum	8.4×10^8	4.2×10^8	4.2×10^7
EC trigger rate for $p > 1$ GeV (kHz)			
e^-	152	82	70
π^-	4.0×10^3	2.2×10^3	1.8×10^3
π^+	0.2×10^3	0.1×10^3	0.1×10^3
$\gamma(\pi^0)$	3	3	0
p	1.6×10^3	0.9×10^3	0.7×10^3
sum	5.9×10^3	3.3×10^3	2.6×10^3
trigger rate for $p < 1$ GeV (kHz)			
sum	2.8×10^3	1.4×10^3	1.4×10^3
EC total trigger rate (kHz)			
total	8.7×10^3	4.7×10^3	4.0×10^3
EC trigger rate per sector (kHz)			
total	290	155	135

Table 6: Calorimeter trigger rates based on ^{48}Ca target. DIS and background rates that enter full coverage of the EC are considered for the resulting trigger rates. Trigger is broken down to $p < 1$ GeV and $p > 1$ GeV particles and for the "low" and the "high" background regions. The total rate for the sum of 30 sectors are shown here. The simulated pion rejection and electron efficiency values are shown in Fig. 29.
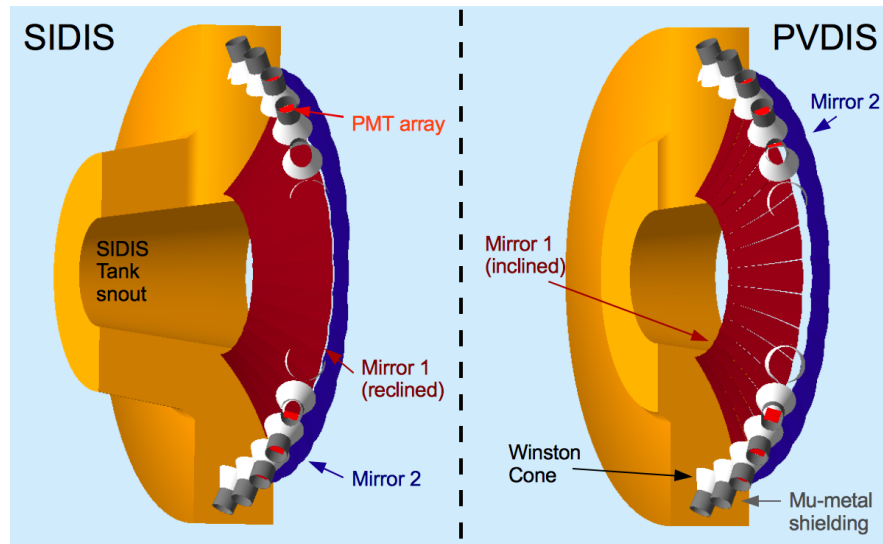
Figure 30: Geant4 cross section of the light gas Cherenkov detector for the SIDIS (left) and PVDIS (right) configurations.
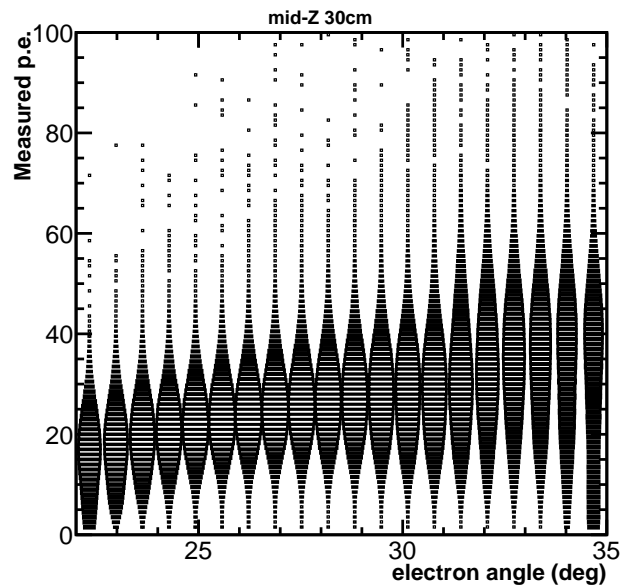
Figure 31: Simulation results for collected photoelectrons for the PVDIS LD$_2$ experiment for the middle of the target.
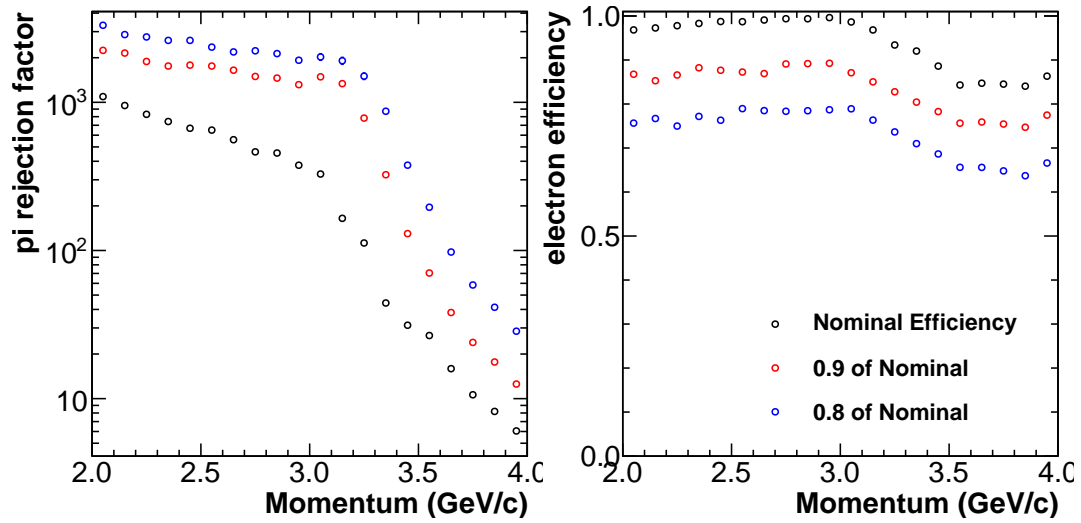
Figure 32: Simulation results for the pion rejection factor and electron detection efficiency for a "nominal" case where π^- rejection is maximized and and minimizing the loss of electrons as well as the $\sim 10\%$ and $\sim 20\%$ e^- loss cases.
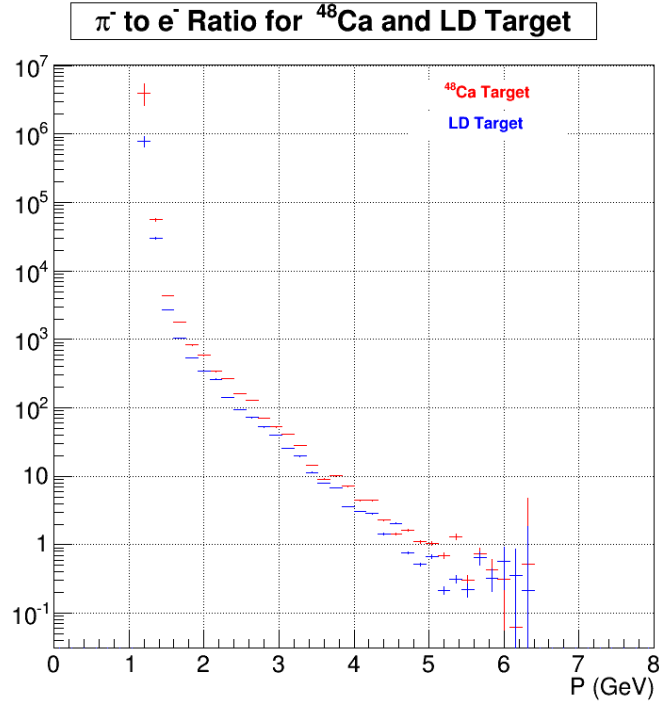
Figure 33: A comparison of π^- to e^- for LD_2 and ^{48}Ca targets. The ratio for ^{48}Ca is about 50% larger.

	Total Rate for p > 0.0 GeV (kHz)	Rate for p > 3.0 GeV (kHz)
DIS	240	73
π^-	5.9×10^5	1.6×10^3
π^+	2.7×10^5	40
$\gamma(\pi^0)$	7.0×10^7	40
p	4.8×10^5	4
Sum	7.1×10^7	1.7×10^3
Trigger Rate from Cherenkov (kHz)		
	Trigger Rate for p > 1.0 GeV (kHz)	Trigger Rate for p > 3.0 GeV (kHz)
DIS	223	66
π^-	193	49
π^+	22	1.6
$\gamma(\pi^0)$	0	0
p	0	0
Sum	438	116
Sum per sector	14.6	3.9

Table 7: Cherenkov trigger rates for ^{48}Ca target at 80 μA is estimated using simulated pion rejection and electron efficiency values from Fig. 32.

5.2.5 Data Acquisition

Due to the large number of channels and the necessity to keep the readout size small, the data acquisition system for SoLID is complex, even for the inclusive, independent-sector running for a PVDIS measurement. To approach this, SoLID utilizes pipelined electronics similar to the Hall D GlueX design. The readout for the calorimeter and Cherenkov is a VME JLAB FADC250 16-channel 12-bit FAC sampling at 250 MHz and a schematic of the FADC crate layout is shown in Fig. 34. VMM3 are currently being tested and will become the standard for GEM readout which is a pipelined readout system that will integrate with rest of the DAQ. A summary of channel and module counts per sector is shown Table 8.
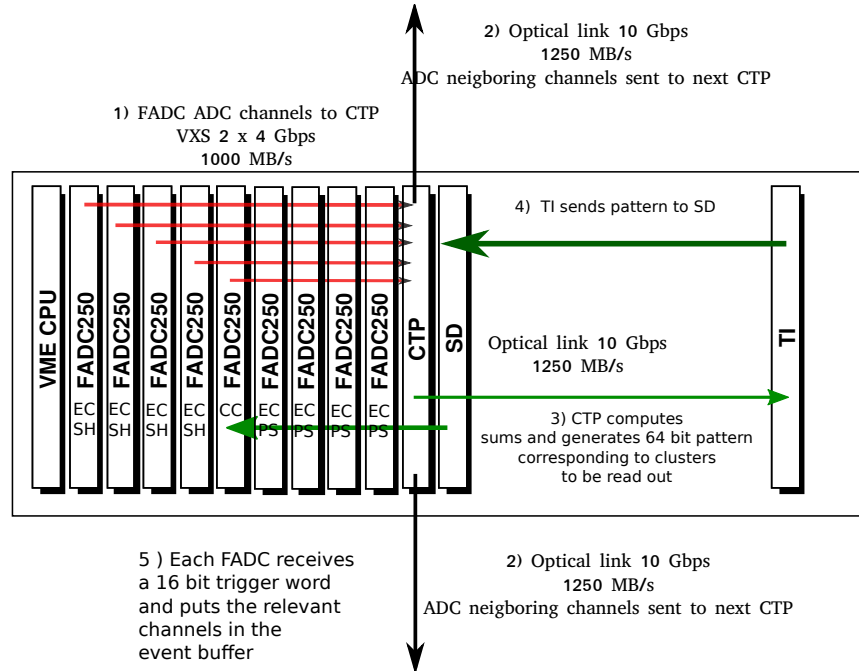
Figure 34: Layout of the FADC crate for the shower and preshower systems. Each crate contains a crate trigger processor (CTP), signal distribution module (SD), and trigger interface (TI).

Detector	Module Type	Number of Channels	Number of Modules
Electromagnetic Calorimeter (EC)	FADC	122	8
Light Gas Cherenkov (GC)	FADC	9	1
GEM	VME	4700	3

Table 8: Detector channel counts for each sector.

For our experiment, we anticipate about a total 155 kHz coincidence trigger, Table 9, for all sectors using both the calorimeter and gas Cherenkov signal compared to the 500 kHz trigger for the LD_2 measurement. We will run the 30 sectors independently requiring about 5 kHz/sector for the primary measurement.

A level 1 trigger can be formed by summing all modules for all sectors simultaneously every 4 ns and sending the signal to the crate trigger processor (CTP). To account for overlapping sectors on the calorimeter plane, neighboring CTPs are connected through optical links to share the overlapping 16 channels. Sup-

Particle	DAQ Coincidence Trigger Rate (kHz)	
	P > 1 GeV	P > 3 GeV
DIS e^-	144	61
π^-	11	7
π^+	0.4	0.2
Sum	155	68
Rate per sector	5.2	2.3

Table 9: Breakdown of coincidence trigger rates (Cherenkov+EM calorimeter) for momentuma > 1 GeV from ^{48}Ca target at $80 \, \mu$A. Also given is the rate for each of the 30 sectors (and 30 independent DAQ systems).

pression will be invoked on hits outside of a cluster. The gas Cherenkov configuration is similar but less complicated as each PMT array is unique to a sector and there is no overlap.

The VMM3 is currently being tested and will become the standard for GEM readout. This allows for a deadtime-less readout of the GEM signals. The DAQ system interfaces with the VMM3 chips to handle triggering of the readout, data transfer, and event building.

The data is then fed to the level 3 farm for data reduction. For this experiment the level 1 event data size is expected to be less than 50 kB with a 200 kHz level 1 rate. Further data reduction will be done correlating detectors such as the GEMs and calorimeter clusters together in space and time. Afterwards, crude track reconstruction must be performed for the GEMs. In particular, this is important for the GEM data rates as the occupancy will be on the order of 10-20%, or $\sim$3000 hits, making full hit recording untenable. See Section 7.2.3 for radiation dose on electronics.

5.3 Polarimetry

A precise determination of the beam polarization is required to relate the asymmetry to the underlying physics measurement. As our statistical precision is about 1%, we require an uncertainty from the polarization better than that. We will utilize two independent techniques to measure this, Compton and Møller polarimetry. The upgrade to the existing Hall A Compton polarimeter is expected to provide a 0.4% precision. The MOLLER collaboration intends to improve precision of the existing Møller polarimeter to 0.4%.

5.4 Tracking, Optics, and Calibration

To precisely determine the kinematics of individual scattering events, tracking must first be performed using the GEM chambers and calorimeter, and then a sufficient optics model must be in place to reconstruct the event. In particular, the momentum p, scattering angle θ, and the scattering vertex along them beamline z must be known to sufficient precision to determine x and Q^2 as well as eliminate background window scattering events or events that originate outside of the target. Due to the relatively high luminosity and large acceptance for the experiment, efficient and fast tracking is important.

The overall background rates for this experiment are generally a factor of 2 smaller than the LD$_2$ experiment and therefore less demanding. As this is an inclusive measurement, tracking only needs to be done across a single sector. Presently, simulations are underway testing several tracking algorithms under the SoLID experimental conditions. These include a detailed model of SoLID and the individual GEM planes as well as a model detailing the ionization and GEM front-end electronics response based on real data [65] implementing an existing framework used for the Super Bigbite project, [66]. Those studies have shown 90% track reconstruction efficiency in occupancies that exceed the worst-case estimates of SoLID.

One additional challenge of the SoLID experiments is to reduce the data rate, as rough tracking must be performed "on the fly". This requires extensive simulation and testing of reconstruction algorithms before the experiment can run. The SoLID collaboration is actively working at realizing this.

Optics models were implemented based on ray-traced tracks in the Geant4 simulation using a field map generated by the Poisson/Superfish package with a realistic coil and yoke geometry. The 0th order terms were based on the trajectories of particles in a uniform field and then deviations were fit using first order polynomials of generic track parameters. It was determined for SoLID in the PVDIS configuration that the momentum resolution is multiple scattering limited and about 1%, the angular resolution is GEM resolution limited and 0.5%, and the beamline vertex resolution of 7 mm. The derived quantities Q^2 and x were 1.5% and 1% respectively.

The calibration of the system requires several steps. First, GEM alignment must be done using "straight through" tracks with the magnetic field off and a combination of a set of thin carbon foils to ensure accurate interaction vertex reconstruction and a sieve to ensure angle reconstruction. Second, we utilize elastic scattering from a liquid hydrogen target and lower the beam energy to 4.4 GeV. The position of the elastic peak provides a point of calibration and the magnetic field can be scanned to provide additional points.

To aid with the determination of radiative effects, independent aluminum targets with $x/X_0 = 1\%$, 5%, and 10% will be included. These will aid in the verification of scattering rate distributions under different radiative conditions and the overall unfolding procedure, which will be limited by the determination of quantity of event bin-migration.

6 Projections, Uncertainties, and Beam Time Request

6.1 Statistical Uncertainty

Our statistical uncertainty is calculated for 68 days at 80 μA on a 93% isotopically pure 2.4 g/cm^2 ^{48}Ca target. The projected statistical uncertainties on A_{PV} for our x and Q^2 bins is shown in Fig. 18. This translates to a sensitivity in a_1 shown in Fig. 14 assuming the standard model values for C_{1i} and C_{2i}. The $Ya_3/2$ term in Eq. 6 is small for our kinematics only contributes to about 5% of the asymmetry and is approximately proportional to the a_1 term due to the small contributions from sea quarks.

6.2 Systematics

The total systematic uncertainties are summarized in Table 10 and discussed in the following subsections.

Effect	Uncertainty [%]
Polarimetry	0.4
$R^{\gamma Z}/R^{\gamma}$	0.2
Pions (bin-to-bin)	0.1-0.5
Charge-symmstric background	<0.1
Radiative Corrections (bin-to-bin)	0.5-0.1
Other corrections including CSV	0.2
pdf uncertainties	0.2
Total systematic	0.6-0.7
Statistics	0.7-1.3

Table 10: Summary of the systematic error contributions to our measurement after correcting for the pion and charge-symmetric backgrounds. Some items (e.g. $R^{\gamma Z}$, CSV, pdf uncertainties) do not impact the experimental uncertainty, but are relevant in the interpretation of the data in terms of flavor dependence of the EMC effect. We have included these uncertainties along with the experimental systematics for purposes of evaluating the sensitivity of the measurement.

6.2.1 Polarimetry

Two independent polarimeters will be deployed for this experiment. A continuous monitoring of the polarization will be done by the upgraded Compton polarimeter, which is anticipated to give 0.4% systematic uncertainty using both the photon and electron detectors. The iron-foil Møller polarimeter will provide an additional measurement periodically, as it is invasive, but with a projected uncertainty of about 0.8%. Recent results from the CREX experiment are already approaching the needed precision, having achieved $dP/P = 0.45\%$ when combining results from the Møller and Compton polarimeters. We assume a 0.4% shared systematic for our measurement.

6.2.2 $R^{\gamma Z}$ uncertainty

Ref. [67] evaluates the impact of a 10% and 20% difference between $R^{\gamma Z}$ and R^{γ} on the parity-violating asymmetry. In a subsequent publication [68], detailed calculations of the impact of target mass effects on the difference between $R^{\gamma Z}$ and R^{γ} were performed and suggest that the expected difference (due to perturbative effects) is at most 4% for the proton in the x range sampled by this proposal (see Figures 9 and 10 of Ref.[68]), corresponding to a 0.2% uncertainty on a_1. Note that while target mass effects approach

4% for the proton, they are smaller for the deuteron (at most 2%) and for ^{48}Ca, yielding a $\sim$0.1% effect on this proposal. There is some additional uncertainty due to the potential difference in non-perturbative contributions to $R^{\gamma Z}$ and R^γ. We apply a 0.2% uncertainty to account for these effects.

6.2.3 Pion Contamination

Our anticipated pion contamination to the electron signal is expected to be no worse than 4% in any given bin based on the combined rejection factors in the Cherenkov and the preshower and shower counters. This is a small effect but still large enough to require a correction to the measured asymmetry. The contamination is worst at the highest x due to the increased difficulty of separating high energy pions from electrons, but better for the higher Q^2 bins at a fixed x due to the relative number of fewer pions at large angle. To make a correction this requires good characterization of the pion contamination and the pion asymmetry.

The pion contamination level can be determined to good accuracy by using the preshower/shower and the gas Cherenkov to cross-check one another. There is a large phase space in which to characterize, including momentum and position, but also drifts over time. A fraction of triggers without the gas Cherenkov will be dedicated to characterize this.

The pion asymmetry in the 6 GeV Hall A PVDIS experiment was measured to be a few times smaller than the LD$_2$ asymmetry [69] but with the same sign. To be conservative, we assume that the π^- asymmetry is zero when estimating the size of the correction on a_1. Under this assumption, we can keep the total pion systematic below 0.5%, if we know the fractional pion contribution at the 10% level and know the π^- asymmetry at the 10 ppm level. Of course in the experiment we will measure the pion asymmetry rather than assuming zero, which will reduce the size of the correction and the associated uncertainty assuming that it is of the same sign as the electron asymmetry.

We will take 300-400 Hz per sector of dedicated pion triggers over the course of the data taking. This rate will provide sufficient statistics to measure asymmetry of the pion background at the <10 ppm level and will provide sufficient statistics to verify the pion contamination rates with a drift on the order of hours. We assign a systematic of 0.1-0.5% bin-to-bin, larger at larger x.

6.2.4 Charge-Symmetric Background

Charge symmetric backgrounds in inclusive electron scattering are generated primarily from π^0 photoproduction and the subsequent decay, $\pi^0 \to e^+ e^- \gamma$. The electrons from this process can not be separated from those coming from DIS, so must be determined empirically via measurements of positron rates.

The charge symmetric background for this experiment was estimated using the model described in Ref. [70], tuned to agree with data taken as part of E03103 (see Fig. 35). The background is $\approx$15% at x=0.25, but decreases rapidly as x increases. This background is not expected to carry a significant asymmetry, but the dilution must be precisely determined to minimize the uncertainty on the final asymmetry. Dedicated measurements will be made with the solenoid polarity reversed to measure the charge symmetric background. At the lowest x, the positron yield should be measured to a relative precision of 1% to minimize impact on the final result. Four days have been have been requested to make measurements of the charge symmetric background: solenoid polarity changes (2 polarity changes, 1 day each including commissioning/checkout with beam), positive polarity production data (2 days).

Further checks of the model used to make the charge symmetric background estimates will be available after the upcoming run of E12-10-008 in Hall C, which will take data on ^{48}Ca at kinematics similar to those in this proposal.
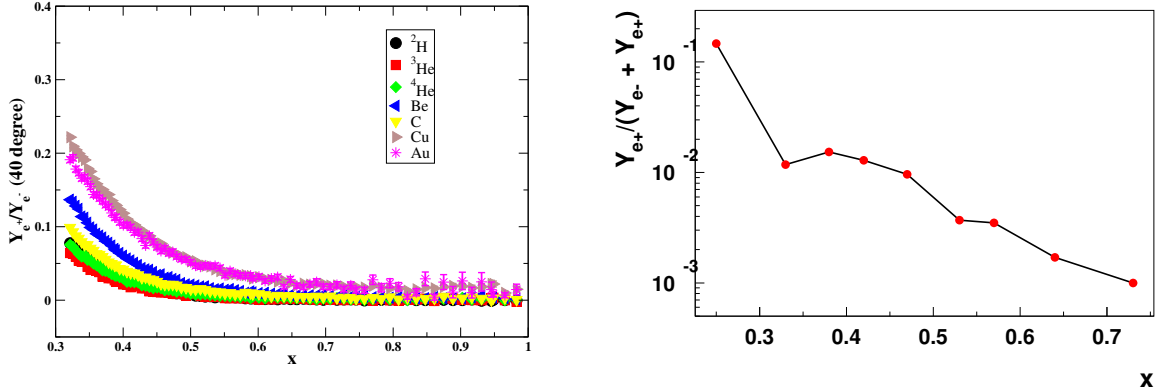
Figure 35: Charge-symmetric background at 5.77 GeV, 40 degrees, from E03-103 [21] (left). Expected charge-symmetric background for this experiment (evaluated at x and Q^2 values corresponding to Fig. 18), predicted using the model in Ref. [70] modified to agree with the Hall C E03-103 data (right).

6.2.5 Radiative Corrections

Several factors need to be applied to extract the PDF-dependent quantities from our measured asymmetry. First, an unfolding procedure will need to be included to account for the hard radiative events. This causes the average Q^2 to be reduced, causes events from lower energy transfer (including resonant) events to become convoluted into the asymmetry. Fortunately, there is good momentum acceptance up to and even beyond elastic events, so these contributions will all be measured to sufficient accuracy within the Q^2 acceptance of the measurement. It was also shown that resonance event asymmetries are in general agreement with quark-hadron duality arguments [71].

The theory for radiative corrections is well understood e.g. [72], though calculations for our kinematics are ongoing by a dedicated working group within the collaboration. Up to 40% of the reconstructed DIS signal will come from resonance or migrated DIS and are worst for the lowest x bins. However, these events have asymmetries that are only a few percent different from the primary asymmetry which makes the corrections relatively small. We claim we can understand the size of the tails to at least 10% relative in the unfolding procedure, and we assign a 0.5%-0.1% bin-to-bin systematic, worse for small x.

The electroweak couplings, C_{iq}, are valid for all energy scales in the absence of radiative loop corrections. With these corrections, in one parameterization they become [32]

$$C_{1u} = \rho'_e \left(-\frac{1}{2} + \frac{4}{3}\hat{\kappa}'_e \hat{s}^2_Z \right) + \lambda' \tag{11}$$

$$C_{1d} = \rho'_e \left(\frac{1}{2} - \frac{2}{3}\hat{\kappa}'_e \hat{s}^2_Z \right) + 2\lambda' \tag{12}$$

$$C_{2u} = \rho_e \left(-\frac{1}{2} + 2\hat{\kappa}_e \hat{s}^2_Z \right) + \lambda_u \tag{13}$$

$$C_{2d} = \rho_e \left(\frac{1}{2} - 2\hat{\kappa}_e \hat{s}^2_Z \right) + \lambda_d \tag{14}$$

with, for $Q^2 \to 0$, $\rho'_e = 0.9887$, $\rho_e = 1.0007$, $\hat{\kappa}'_e = 1.0038$, $\hat{\kappa}_e = 1.0297$, $\lambda' = -1.8 \times 10^{-5}$, $\lambda_u =$

-0.0118, $\lambda_d = 0.0029$, and $\hat{s}_Z^2 = \sin^2 \theta_W = 0.2312$. These are being calculated for our kinematics and are not likely to change in a way that is sensitive to this experiment.

6.2.6 Hadronic and Nuclear Uncertainties

There are potential contributions that can arise from higher order hadronic effects. Higher twist, charge symmetry violation (which mimics our isovector EMC effect in our signal), PDF uncertainties, and free PDF nuclear-model uncertainties can all potentially interfere with the extraction of a signal. Lattice calculations indicate very small CSV contributions [73], and these effects will be greatly constrained by approved measurements, within and outside of the SoLID program.

Charge symmetry violation will be measured in LD_2 to better precision than ours across the same kinematic range using the same apparatus, as described in Ref. [50] and are likely to be smaller than the proposed isovector EMC effect. If charge symmetry violation is found to be large in LD_2 or if the measurement here is found to be unexpectedly large, that may motivate a proposal similar to this one, but on ^{40}Ca. At present we assign no systematic uncertainty to charge symmetry violating effects.

$R = \sigma_L/\sigma_T$ has been determined for proton and deuterium DIS over a broad kinematic range, e.g. Ref. [74], and is about 0.2 for our kinematics. For our measurement of an asymmetry, the effects of this will mostly cancel, though one potential concern for this proposal is the nuclear dependence of of R. It has been suggested that these may be on the order of a few percent for our kinematics [75], which is negligibly small for our experiment due to cancellations and we ignore it.

For a symmetric target, specific higher twist effects can contribute in A_{PV} even though other Q^2 dependent effects such as the DGLAP evolution are highly suppressed. If they do turn out to be significant, the LD_2 measurement will provide constraints which then can be used as corrections to our measurement. For a 10% variation on a symmetric target at $Q^2 = 5$ GeV^2, these appear as a 0.5% correction to A_{PV} [67]. The LD_2 experiment uses a combination of 11 GeV and 6.6 GeV beam with the kinematic reach from 3 - 8 GeV^2 and as these effects to first order scale with $1/Q^2$, this provides a useful lever arm. We will be at high Q^2 kinematics and assign a shared systematic of 0.2% to our measurement.

6.2.7 Uncertainties from Free Parton Distributions

If the free parton distributions are not well constrained for our kinematics, it presents an effective systematic when comparing the measured asymmetry to the expectation for a flavor-independent EMC effect. While individual flavors are often shown to be well constrained by themselves, we are pursuing an unusual combination which requires careful consideration. We note that if flavor-dependent nuclear corrections are extremely large, this will yield a correction to the extracted d-quark distributions taken from data on the deuteron or the comparison of ^{3}H and ^{3}He. However, since we are looking at deviations in the size of the EMC effect for up and down quarks, we can begin with extractions that do not allow for a large flavor dependence.

At low x, the dominant uncertainty comes from the size of the sea quark contributions. Based on the CJ12 pdf [76], this yields an uncertainty on a_1 of 0.002 for our lowest x value, where the statistical uncertainty is large, and is $\approx$0.001 or below for larger x values. This yields a negligible contribution to the overall sensitivity of the measurement.

At larger x values, the dominant contribution to the a_1 uncertainty comes from uncertainty in the d-quark distribution. The recently published MARATHON F_{2n}/F_{2p} [45] data, converted to $d(x)/u(x)$ in leading order, yields an uncertainty on $d(x)/u(x)$ of approximately 0.025 over the x range of the proposed measurements, as shown in Fig. 36. By the time of the PVEMC run, we expect to have measurements of similar precision from the PVDIS measurement on hydrogen, and even better precision for all but our largest x value from the BONUS12 experiment [77]. Current pdf analyses quote even smaller uncertainties,
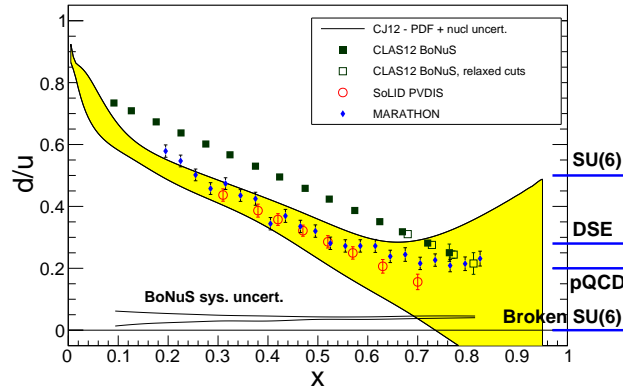
Figure 36: Anticipated data for measurements on d/u, see text for references. The constraints provided by these data will allow for accurate tests of an isovector EMC effect at larger x. The leading order ratio d/u was extracted from recently published MARATHON [45] F_2^n/F_2^p results are also shown

with the CJ15 analysis providing an uncertainty on $d(x)/u(x)$ of ~0.006 for our x range even without the MARATHON data. However, global analyses are somewhat sensitive to the assumptions of the analysis and details of the data sets included, and so it is not clear that this can be taken as a reliable estimate at this point in time. For this proposal, we assume that the uncertainty on $d(x)/u(x)$ in our x region will be 0.01 - comparable to the combined precision of the experimental projections shown in Fig. 36, but larger that what is quoted by present pdf analyses. This translates into an uncertainty of 0.02% for the comparison of the measured asymmetry to the expectation for a flavor-independent EMC effect.

6.2.8 Corrections Beyond Leading Order

Interpreting the data including next-to-leading order terms should not significantly affect this asymmetry. Because the gluon is spin-0, the additional α_s vertex is not spin dependent. Additionally, the gluon couples to quark color-charge and is blind to quark flavor, so there will be no flavor dependence arising from the NLO terms. The Feynman diagrams for the NLO terms are shown in Fig. 37. The vertex correction and quark scattering terms will serve to obscure slightly the kinematics of the observed event. Finally, the quark scattering and gluon fusion term will dilute the signal, but is calculable. We are in discussion with theorists on completing these calculations in NLO.
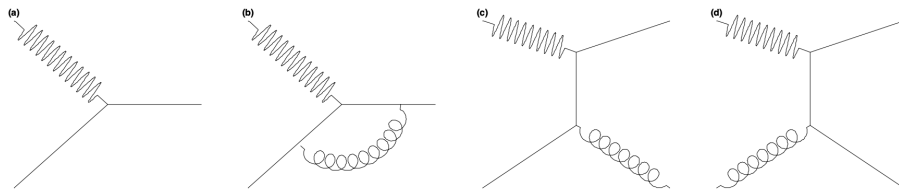

Figure 37: LO and NLO Feynman diagrams for DIS. (a) Leading order diagram. (b) Vertex correction (c) quark scattering (d) gluon fusion.

6.2.9 Beam Parameters

Corrections to the measured asymmetry from helicity-correlated beam parameters are likely to be small due to the existing excellent beam quality at Jefferson Lab, the level of control at systematically reducing these errors, such as the double Wien filter, and the relative size of our asymmetry, which is on the order of 10^{-4} compared to the 10^{-6} level for experiments such as Qweak and PREX. Corrections are likely to be on the 0.1% level.

We have estimated an upper limit for beam normal spin asymmetry for ^{48}Ca using semi-empirical formula based on results from CREX experiment and found out to be -100 ppm. We are expecting less than 5% transverse leakage during production running. The azimuthal symmetry of the SoLID detectors will provide symmetry suppression factor of about 500. This was based on observed symmetry suppression during Qweak experiment. Based on transverse leakage and symmetry suppression factor we are expecting about -0.01 ppm residual beam normal spin asymmetry which is a negligible effect for a PVDIS asymmetry measurement.

6.3 Beam Time Request

We request 68 days of production data at 11 GeV at 80 μA with full beam polarization. We also request time for commissioning, calibration and background runs, and polarimetry, summarized in Table 11.

Table 11: Beam time request for this experiment.The positive polarity running includes 1 day per polarity change of the SoLID magnet.

	Time (days)	E (GeV)	Current (μA)
^{48}Ca Production	68	11	80
Optics	2	4.4	Up to 80
Positive polarity	4	11	80
Moller Polarimetry	4	11	2
Commissioning	5	11	Up to 80
Total	83		

7 Radiation Dose and Shielding Status

Radiation is generated from the ^{48}Ca target by direct electron beam interactions as well as from scattered electrons undergoing secondary interactions in the hall. The iron core of the solenoidal magnet provides self shielding for high energy neutrons and will help to reduce the site boundary radiation budget. There are more extensive radiation and shielding studies for all SoLID experiments underway by the collaboration to minimize the radiation to the hall and to site boundary. This section will provide a comprehensive summary about the radiation dose for various subsystems projected for the proposed experiment.

7.1 Site Boundary Dose Comparison

During the design of PREX and CREX experiments, we made progress in developing a more realistic Geant4 simulation to estimate the radiation dose. After the conclusion of PREX and CREX, we compared our updated simulations with site boundary dose measurements. These measurements have shown that Geant4 simulations have consistently overestimated the expected boundary dose as shown in the Table 12. Based on the Geant4 simulations we conducted, we have estimated that boundary dose during our proposal beam period to be about 2.5 mrem without dedicated sky-shine shielding implemented. These numbers obtained from simulations for ^{48}Ca and are *not scaled from PVDIS-LD2*. The main simulation software utilized for PVEMC studies is the same as the simulation used for PREX/CREX, MOLLER and SoLID-PVDIS experiments. The final site boundary dose will be further reduced after the SoLID shielding design is further optimized.

Experiment	Top of the Hall Neutron Dose (m^{-2})	Estimated Boundary DOSE (mrem)	Measured Boundary DOSE (mrem)
PREX-I	4.50E+12	4.2	1.3
PREX-II	5.80E+12	2.0	1.2
CREX	1.50E+13	1.8	1.0
LD-PVDIS 6 GeV	1.90E+12	0.7	n/a
LD-PVDIS 11 GeV	3.40E+12	1.3	n/a
^{48}Ca-PVDIS 11 GeV	6.00E+12	2.5	n/a

Table 12: Neutron dose at the top of the hall enclosure and site boundary dose were estimated using Geant4 simulations for previously ran PREX-I, PREX-II, CREX and LD-PVDIS 6 GeV experiments. The RAD-CON has measured site boundary dose for these experiments. The Geant4 simulations we used has consistently overestimated the RADCON site boundary dose measurements for these experiments.

7.2 Radiation Dose in the Hall

Based on the simulations completed for the SoLID 2019 director's review, the SoLID-PVDIS configuration does not present high radiation levels for the electronics in the Hall. For reference, we compare radiation budget from the 12% ^{48}Ca target to the approved LD$_2$ measurement in Table 13. Based on this, PVEMC running with the ^{48}Ca target will have approximately 2.5 times the total integrated radiation dose to the hall (see column 2, Table 13) .

To estimate the radiation dose for systems in the hall, we start by taking the calculation of the radiation in the Hall for PVDIS running at 100μA for 2000 hours, as shown in figure 38 [78]. This is a significant
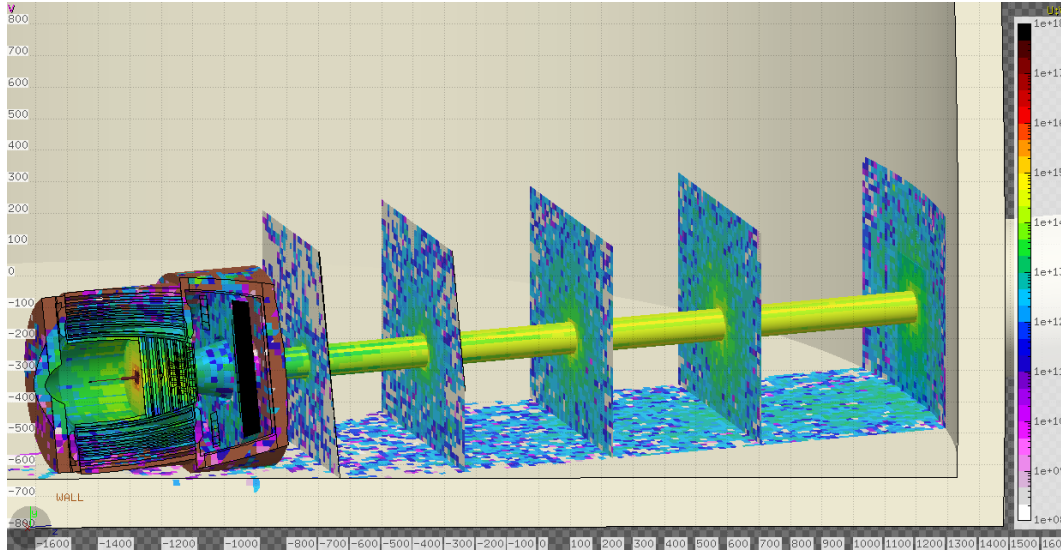
Figure 38: Radiation dose for PVDIS with deuterium target running at $100\mu A$ for 2000 hours, [78]. The color scale shows (1 MeV equiv Neutron)/cm^2 dose levels.

Experiment	Hall (rem/h)	Ceiling (rem/h)
^{48}Ca at 80 uA, 68 days	25.2	2.4
LD2 at 50 uA, 60 days	10.2	1.2
Increase (%)	150	100

Table 13: Radiation dose in the hall and at the ceiling is estimated for ^{48}Ca and deuterium (LD2) targets. The dose increase for ^{48}Ca running is also shown at the bottom row.

overestimate for the LD2 current and run time, and even scaling up for the higher current and longer radiation length of the ^{48}Ca target, it is an overestimate for PVEMC. As such, we use this as a conservative basis for estimating local radiation dose on electronics and other hardware in the hall enclosure. The areas surrounding the beamline downstream of the SoLID apparatus have the highest observed radiation, while the solenoid magnet provides self-shielding, significantly reducing the radiation into the hall. We discuss the impact of the radiation in the hall on the experimental equipment in the following subsections.

7.2.1 Radiation Dose in the Calorimeter

The luminosity for this experiment is about 2×10^{37} Hz/cm^2 (calculated per nucleus), or a factor of 3 smaller per-nucleon than the LD$_2$ measurement. The estimated radiation dose on the calorimeter from the proposed PVEMC running is about 37 kRad. This would be additional dose on top of the 200 kRad from the running of the currently approved SoLID program (both PVDIS and non-parity measurements). This measurement represents a relatively small increase in the total radiation dose, and the total dose for the full program of measurements is below 60% of the calorimeter design specification of 400 kRad per Shashlik calorimeter module.

7.2.2 Superconducting Coil Radiation Dose

Superconducting coil degradation is expected at doses above 2×10^{17} (1 MeV equiv Neutron)/cm^2 [78]. The total dose on coils from the LD2 and ^{48}Ca running will be a factor of $\sim$1000 below this estimated threshold for degradation. While we do not know the current accumulated dose to the coils, it is unlikely to be anywhere near this level as the CLEO maximum luminosity was 10^{32} cm$^{-2}s^{-1}$, seven orders of magnitude below the SoLID-PVDIS luminosity of 10^{39} cm$^{-2}s^{-1}$

7.2.3 Electronics Radiation Dose

Figure 39 shows the radiation doses at which damage is expected to occur in a variety of electronic devices. Non radiation-hard electronics are not expected to suffer damage below doses of 1×10^{13} (1 MeV equiv Neutron)/cm^2. That level of localized dose is only seen around the downstream beamline area according to the FLUKA simulation [78] estimates shown in Figure 38. Most of the electronics will be placed away from these high-radiation areas and will be placed in dedicated shielding enclosures, reducing the exposure to well below the level at which damage might be expected to occur. Certain GEM electronics will be mounted in the region after the baffles with the GEM detectors but the localized dose in this region is also below the damage threshold for 'Not Radiation-Hard' electronics.
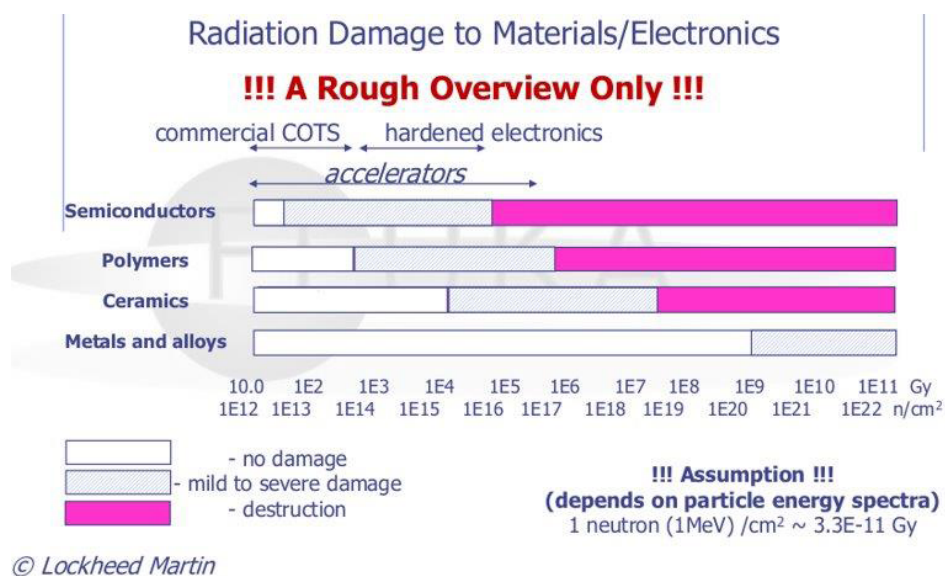

Figure 39: Radiation dose in (1 MeV equiv Neutron)/cm^2 and tolerance of different electronics.

There are more extensive radiation and shielding studies for all SoLID experiments underway by the collaboration to minimize the radiation to the hall and to site boundary. The ^{48}Ca setup will be an integral part of these simulations. Based on preliminary radiation dose study quoted above, the local dose on electronics for both LD2 and ^{48}Ca running will be about a factor 1000 lower when local shielding measures are implemented. We will update the simulations with electronic shielding enclosures to estimate the reduction in dose due using the optimized shielding enclosures when a final shielding design is completed.

A Quark Parton Model

In Eq. 6 higher order corrections for Y_1 and Y_3 were neglected and the Callan-Gross relation $F_2 = 2xF_1$ was invoked. Here we follow the convention of Ref. [67]. We define

$$
R^{\gamma(\gamma Z)} \equiv \frac{\sigma_L^{\gamma(\gamma Z)}}{\sigma_T^{\gamma(\gamma Z)}} = r^2 \frac{F_2^{\gamma(\gamma Z)}}{F_1^{\gamma(\gamma Z)}} - 1 \tag{15}
$$

$$
r^2 = 1 + \frac{Q^2}{\nu} = 1 + \frac{4M^2 x^2}{Q^2} \tag{16}
$$

The full parity-violating asymmetry is in terms of the structure functions $F_1^\gamma(\gamma Z)$ and $F_2^\gamma(\gamma Z)$

$$
A_{\mathrm{PV}} = -\left(\frac{G_F Q^2}{4\sqrt{2}\pi\alpha}\right) \frac{g_A^e \left(2xyF_1^{\gamma Z} - 2\left[1 - 1/y + xM/E\right]F_2^{\gamma Z}\right) + g_V^e x(2-y)F_3^{\gamma Z}}{2xyF_1^\gamma - 2\left[1 - 1/y + xM/E\right]F_2^\gamma} \tag{17}
$$

We can then write it in the reduced from by

$$
A_{\mathrm{PV}} = -\left(\frac{G_F Q^2}{4\sqrt{2}\pi\alpha}\right) \left[g_A^e Y_1 \frac{F_1^{\gamma Z}}{F_1^\gamma} + \frac{g_V^e}{2} Y_3 \frac{F_3^{\gamma Z}}{F_1^\gamma}\right] \tag{18}
$$

with

$$
Y_1 = \frac{1 + (1-y)^2 - y^2\left(1 - r^2/(1+R^{\gamma Z})\right) - 2xyM/E}{1 + (1-y)^2 - y^2\left(1 - r^2/(1+R^\gamma)\right) - 2xyM/E}\left(\frac{1 + R^{\gamma Z}}{1 + R^\gamma}\right) \tag{19}
$$

$$
Y_3 = \frac{1 - (1-y)^2}{1 + (1-y)^2 - y^2\left(1 - r^2/(1+R^\gamma)\right) - 2xyM/E}\left(\frac{r^2}{1 + R^\gamma}\right) \tag{20}
$$

and

$$
F_1^\gamma = \frac{1}{2}\sum_i e_i^2\left(q_i(x) + \bar{q}_i(x)\right); F_2^\gamma = 2xF_1^\gamma, \tag{21}
$$

$$
F_1^{\gamma Z} = \sum_i e_i g_V^i\left(q_i(x) + \bar{q}_i(x)\right); F_2^{\gamma Z} = 2xF_1^{\gamma Z}, \tag{22}
$$

$$
F_3^{\gamma Z} = 2\sum_i e_i g_A^i\left(q_i(x) - \bar{q}_i(x)\right). \tag{23}
$$

References

[1] I. C. Cloet, W. Bentz, and A. W. Thomas. Isovector EMC effect explains the NuTeV anomaly. *Phys. Rev. Lett.*, 102:252301, 2009.

[2] Ian C. Cloet and Gerald A. Miller. Nucleon form factors and spin content in a quark-diquark model with a pion cloud. *Phys. Rev. C*, 86:015208, 2012.

[3] John Arrington. Short-range correlations and their implications for isospin-dependent modification of nuclear quark distributions. *EPJ Web Conf.*, 113:01011, 2016.

[4] E. P. Segarra, A. Schmidt, T. Kutz, D. W. Higinbotham, E. Piasetzky, M. Strikman, L. B. Weinstein, and O. Hen. Neutron Valence Structure from Nuclear Deep Inelastic Scattering. *Phys. Rev. Lett.*, 124(9):092002, 2020.

[5] B. Schmookler et al. Modified structure of protons and neutrons in correlated pairs. *Nature*, 566(7744):354–358, 2019.

[6] J. Arrington and N. Fomin. Searching for flavor dependence in nuclear quark behavior. *Phys. Rev. Lett.*, 123(4):042501, 2019.

[7] E. P. Segarra, J. R. Pybus, F. Hauenstein, D. W. Higinbotham, G. A. Miller, E. Piasetzky, A. Schmidt, M. Strikman, L. B. Weinstein, and O. Hen. Short-Range Correlations and the Nuclear EMC Effect in Deuterium and Helium-3. *arXiv:2006.10249*, 2020.

[8] E. P. Segarra et al. The CLAS12 Backward Angle Neutron Detector (BAND). *Nucl. Instrum. Meth. A*, 978:164356, 2020.

[9] X. G. Wang, A. W. Thomas, and W. Melnitchouk. Do short-range correlations cause the nuclear EMC effect in the deuteron? *Phys. Rev. Lett.*, 125(26):262002, 2021.

[10] C. Cocuzza, C. E. Keppel, H. Liu, W. Melnitchouk, A. Metz, N. Sato, and A. W. Thomas. Isovector EMC Effect from Global QCD Analysis with MARATHON Data. *Phys. Rev. Lett.*, 127(24):242001, 2021.

[11] John Arrington, Aji Daniel, Donal Day, Nadia Fomin, Dave Gaskell, and Patricia Solvignon. A detailed study of the nuclear dependence of the EMC effect and short-range correlations. *Phys. Rev.*, C 86:065204, 2012.

[12] I. C. Cloët et al. Exposing Novel Quark and Gluon Effects in Nuclei. *J. Phys. G*, 46(9):093001, 2019.

[13] J. Arrington, A. Daniel, N. Fomin, and D. Gaskell. Detailed studies of the nuclear dependence of F2 in light nuclei. JLab experiment E12-10-008, 2010.

[14] L. Weinstein et al. Semi-Inclusive Deep Inelastic Scattering Measurement of A=3 Nuclei with CLAS12 in Hall B. JLab experiment C12-21-004 (conditionally approved), 2021.

[15] I. C. Cloet, W. Bentz, and A. W. Thomas. Parity-violating DIS and the flavour dependence of the EMC effect. *Phys. Rev. Lett.*, 109:182301, 2012.

[16] Donald F. Geesaman, K. Saito, and Anthony William Thomas. The nuclear EMC effect. *Ann. Rev. Nucl. Part. Sci.*, 45:337–390, 1995.

[17] P. R. Norton. The EMC effect. *Rept. Prog. Phys.*, 66:1253–1297, 2003.

[18] Simona Malace, David Gaskell, Douglas W. Higinbotham, and Ian Cloet. The Challenge of the EMC Effect: existing data and future directions. *Int. J. Mod. Phys. E*, 23(08):1430013, 2014.

[19] D. Dutta, J. C. Peng, I. C. Cloet, and D. Gaskell. Pion-induced Drell-Yan processes and the flavor-dependent EMC effect. *Phys. Rev. C*, 83:042201, 2011.

[20] J. Arrington, D. W. Higinbotham, G. Rosner, and M. Sargsian. Hard probes of short-range nucleon-nucleon correlations. *Prog. Part. Nucl. Phys.*, 67:898–938, 2012.

[21] J. Seely et al. New measurements of the EMC effect in very light nuclei. *Phys. Rev. Lett.*, 103:202301, 2009.

[22] N. Fomin et al. New measurements of high-momentum nucleons and short-range structures in nuclei. *Phys. Rev. Lett.*, 108:092502, 2012.

[23] John Arrington, Nadia Fomin, and Axel Schmidt. Progress in understanding short-range structure in nuclei: an experimental perspective. *arXiv:2203.02608*, 3 2022.

[24] O. Hen, G. A. Miller, E. Piasetzky, and L. B. Weinstein. Nucleon-Nucleon Correlations, Short-lived Excitations, and the Quarks Within. *Rev. Mod. Phys.*, 89(4):045002, 2017.

[25] J. T. Londergan, J. C. Peng, and A. W. Thomas. Charge Symmetry at the Partonic Level. *Rev. Mod. Phys.*, 82:2009–2052, 2010.

[26] J. J. Aubert et al. The ratio of the nucleon structure functions $F2_n$ for iron and deuterium. *Phys. Lett. B*, 123:275–278, 1983.

[27] J. Gomez et al. Measurement of the A-dependence of deep inelastic electron scattering. *Phys. Rev. D*, 49:4348–4372, 1994.

[28] L. B. Weinstein, E. Piasetzky, D. W. Higinbotham, J. Gomez, O. Hen, and R. Shneor. Short Range Correlations and the EMC Effect. *Phys. Rev. Lett.*, 106:052301, 2011.

[29] R. Subedi et al. Probing Cold Dense Nuclear Matter. *Science*, 320:1476–1478, 2008.

[30] I. Korover et al. Probing the Repulsive Core of the Nucleon-Nucleon Interaction via the ^{4}He(e,e'pN) Triple-Coincidence Reaction. *Phys. Rev. Lett.*, 113(2):022501, 2014.

[31] M. Duer et al. Direct Observation of Proton-Neutron Short-Range Correlation Dominance in Heavy Nuclei. *Phys. Rev. Lett.*, 122:172502, 2019.

[32] J. Beringer et al. Review of Particle Physics (RPP). *Phys. Rev. D*, 86:010001, 2012. Section 10,Electroweak model and constraints on new physics.

[33] G. P. Zeller et al. A Precise Determination of Electroweak Parameters in Neutrino Nucleon Scattering. *Phys. Rev. Lett.*, 88:091802, 2002. [Erratum: Phys.Rev.Lett. 90, 239902 (2003)].

[34] E. A. Paschos and L. Wolfenstein. Tests for Neutral Currents in Neutrino Reactions. *Phys. Rev. D*, 7:91–95, 1973.

[35] http://home.fnal.gov/~gzeller/nutev.html.

[36] I. Schienbein, J. Y. Yu, C. Keppel, J. G. Morfin, F. Olness, and J. F. Owens. Nuclear parton distribution functions from neutrino deep inelastic scattering. *Phys. Rev. D*, 77:054013, 2008.

[37] I. Schienbein, J. Y. Yu, K. Kovarik, C. Keppel, J. G. Morfin, F. Olness, and J. F. Owens. PDF Nuclear Corrections for Charged and Neutral Current Processes. *Phys. Rev. D*, 80:094004, 2009.

[38] K. Kovarik, I. Schienbein, F. I. Olness, J. Y. Yu, C. Keppel, J. G. Morfin, J. F. Owens, and T. Stavreva. Nuclear Corrections in Neutrino-Nucleus DIS and Their Compatibility with Global NPDF Analyses. *Phys. Rev. Lett.*, 106:122301, 2011.

[39] Daniel de Florian, Rodolfo Sassot, Pia Zurita, and Marco Stratmann. Global Analysis of Nuclear Parton Distributions. *Phys. Rev. D*, 85:074028, 2012.

[40] Hannu Paukkunen and Carlos A. Salgado. Compatibility of neutrino DIS data and global analyses of parton distribution functions. *JHEP*, 07:032, 2010.

[41] Hannu Paukkunen and Carlos A. Salgado. Agreement of Neutrino Deep Inelastic Scattering Data with Global Fits of Parton Distributions. *Phys. Rev. Lett.*, 110(21):212301, 2013.

[42] B. Z. Kopeliovich, J. G. Morfin, and Ivan Schmidt. Nuclear Shadowing in Electro-Weak Interactions. *Prog. Part. Nucl. Phys.*, 68:314–372, 2013.

[43] D. Dutta, D. Gaskell, K. Hafidi, et al. Precise Measurement of pi+/pi- Ratios in Semi-inclusive Deep Inelastic Scattering Part II: Unraveling the Flavor Dependence of the EMC Effect. JLab Proposal PR12-09-004, 2009.

[44] Iraj Ruhi Afnan, Francois Rene Pierre Bissey, J. Gomez, A. T. Katramatou, Simonetta Liuti, W. Melnitchouk, G. G. Petratos, and Anthony William Thomas. Deep inelastic scattering from A = 3 nuclei and the neutron structure function. *Phys. Rev. C*, 68:035201, 2003.

[45] D. Abrams et al. Measurement of the Nucleon F_2^n/F_2^p Structure Function Ratio by the Jefferson Lab MARATHON Tritium/Helium-3 Deep Inelastic Scattering Experiment. *arXiv:2104.05850*, 2021.

[46] Sergey A. Kulagin and R. Petti. Global study of nuclear structure functions. *Nucl. Phys. A*, 765:126–187, 2006.

[47] S. A. Kulagin and R. Petti. Structure functions for light nuclei. *Phys. Rev. C*, 82:054614, 2010.

[48] E. P. Segarra et al. Nucleon off-shell structure and the free neutron valence structure from A=3 inclusive electron scattering measurements. *arXiv:2104.07130*, 2021.

[49] S. I. Alekhin, S. A. Kulagin, and R. Petti. Nuclear effects in the deuteron and global QCD analyses. *arXiv:2203.07333*, 3 2022.

[50] P. Souder et al. Precision Measurement of Parity-Violation in Deep Inelastic Scattering Over a Broad Kinematic Range. JLab experiment E12-10-007, 2010.

[51] Andreas Aste, Cyrill von Arx, and Dirk Trautmann. Coulomb distortion of relativistic electrons in the nuclear electrostatic field. *Eur. Phys. J. A*, 26:167–178, 2005.

[52] P. Gueye et al. Coulomb distortion measurements by comparing electron and positron quasielastic scattering off C-12 and Pb-208. *Phys. Rev. C*, 60:044308, 1999.

[53] I. Cloet. private communication.

[54] R. B. Wiringa, R. Schiavilla, Steven C. Pieper, and J. Carlson. Nucleon and nucleon-pair momentum distributions in $A \leq 12$ nuclei. *Phys. Rev. C*, 89(2):024305, 2014.

[55] Jan Fredrich et al. COMPASS++/AMBER: Proposal for Measurements at the M2 beam line of the CERN SPS Phase-1: 2022-2024. *CERN-SPSC-2019-022 ; SPSC-P-360*, 2019.

[56] B. Adams et al. Letter of Intent: A New QCD facility at the M2 beam line of the CERN SPS (COMPASS++/AMBER). *arXiv:1808.00848*, 8 2018.

[57] B. Adams et al. Proposal for Measurements at the M2 beam line of the CERN SPS – Phase-1, 2019.

[58] `http://hallaweb.jlab.org/12GeV/SoLID/download/doc/solid_precdr.pdf`.

[59] J. Pumplin, D. R. Stump, J. Huston, H. L. Lai, Pavel M. Nadolsky, and W. K. Tung. New generation of parton distributions with uncertainties from global QCD analysis. *JHEP*, 07:012, 2002.

[60] D. E. Wiser. Ph.D Thesis, University of Wisconsin-Madison, 1977.

[61] J. Arrington, D. Day, D. Higinbotham, and P. Solvignon. Three-nucleon short range correlations studies in inclusive scattering for $0.8 < Q^2 < 2.8(GeV/c)^2$. JLab experiment E08-014, 2008.

[62] S. Riordan et al. Parity-violating measurement of the weak charge distribution of 48Ca to 0.02 fm accuracy. JLab experiment E12-12-004, 2012.

[63] D. Meekins. private communication.

[64] C. W. de Jager et al. The Super-Bigbite Spectrometer for Jefferson Lab Hall A, 2010. `https://userweb.jlab.org/~mahbub/HallA/SBS/SBS-CDR_New.pdf`.

[65] G.M. Urciuli, M. Capogni, and E. Cisbani. Note on GEM digitiation modeling. `http://www.iss.infn.it/cisbani/atmp/gemc/code/`.

[66] G. Cates, K. deJager, J. LeRose, B. Wojtsekhowski, et al. Progress Report on the Super-Bigbite Project, 2011. `http://hallaweb.jlab.org/12GeV/SuperBigBite/SBS_CDR/Response_TR2.pdf`.

[67] T. Hobbs and W. Melnitchouk. Finite-Q^2 corrections to parity-violating DIS. *Phys. Rev. D*, 77:114023, 2008.

[68] L. T. Brady, A. Accardi, T. J. Hobbs, and W. Melnitchouk. Next-to leading order analysis of target mass corrections to structure functions and asymmetries. *Phys. Rev. D*, 84:074008, 2011. [Erratum: Phys.Rev.D 85, 039902 (2012)].

[69] P. E. Reimer, K. Paschke, and X. Zheng. Precision Measurement of the Parity-Violating Asymmetry in Deep Inelastic Scattering off Deuterium using Baseline 12 GeV Equipment in Hall C. JLab proposal PR12-07-102, 2007.

[70] P. Bosted. Pair-Symmetric and Pion Backgrounds for EG1b. `http://www.jlab.org/Hall-B/notes/clas_notes04/2004-005.pdf`.

[71] D. Wang et al. Measurements of Parity-Violating Asymmetries in Electron-Deuteron Scattering in the Nucleon Resonance Region. *Phys. Rev. Lett.*, 111(8):082501, 2013.

[72] Luke W. Mo and Yung-Su Tsai. Radiative Corrections to Elastic and Inelastic e p and mu p Scattering. *Rev. Mod. Phys.*, 41:205–235, 1969.

[73] I. C. Cloet et al. Charge Symmetry Breaking in Spin Dependent Parton Distributions and the Bjorken Sum Rule. *Phys. Lett. B*, 714:97–102, 2012.

[74] L. W. Whitlow, E. M. Riordan, S. Dasu, Stephen Rock, and A. Bodek. Precise measurements of the proton and deuteron structure functions from a global analysis of the SLAC deep inelastic electron scattering cross-sections. *Phys. Lett. B*, 282:475–482, 1992.

[75] Vadim Guzey, Lingyan Zhu, Cynthia E. Keppel, M. Eric Christy, Dave Gaskell, Patricia Solvignon, and Alberto Accardi. Impact of nuclear dependence of $R = \sigma_L/\sigma_T$ on antishadowing in nuclear structure functions. *Phys. Rev. C*, 86:045201, 2012.

[76] J. F. Owens, A. Accardi, and W. Melnitchouk. Global parton distributions with nuclear and finite-Q^2 corrections. *Phys. Rev. D*, 87(9):094012, 2013.

[77] S. Bueltmann et al. The Structure of the Free Neutron at Large x-Bjorken. JLab experiment E12-06-113, 2006.

[78] Lorenzo Zana. `https://solid.jlab.org/DocDB/0002/000228/002/Zana_SoLID_DirReview_Sept2019_Radiation_and_Activation.pdf`.